

Reynolds-Averaged Two-Fluid Model prediction of moderately dilute fluid-particle flow over a backward-facing step

M. Riella*, R. Kahraman, G.R. Tabor

College of Engineering, Mathematics and Physical Sciences, University of Exeter, North Park Road, Exeter EX4 4QF, UK

Abstract

In this work a Reynolds-Averaged two-fluid fully coupled model (RA-TFM) for modelling of turbulent fluid-particle flow is implemented in OpenFOAM and applied to a vertically orientated backward-facing step. Three particle classes with varying mass loadings (10-40%) and different Stokes number are investigated. Details of the implementation and solution procedure are provided with special attention given to challenging terms. The prediction of mean flow statistics are in good agreement with the data from literature and show a distinct improvement over current model predictions. This improvement was due to the separation of the particle turbulent kinetic energy k_p , and the granular temperature Θ_p , in which the large scale correlated motion and small scale uncorrelated motion are governed by separate transport equations. For each case simulated in this work, turbulence attenuation was accurately predicted, a finding that is attributed to separate coupling terms in both transport equations of k_p and ε_p .

Keywords: Turbulence attenuation, Backward-facing step, RA-TFM, OpenFOAM

*Corresponding author

Email address: mjr214@exeter.ac.uk (M. Riella)

1. Introduction

Modulation of turbulence is a complex two-way coupled phenomenon [14] and can be caused by fluid-particle interaction and/or particle-wall interaction. Modulation can result in an increase in the fluid-phase fluctuating velocities [24] due to particle vortex shedding [40], which is caused by a large particle Reynolds number, Re_p . Conversely, modulation of turbulence can result in the reduction of fluid-phase fluctuating velocities, i.e. attenuation. This behaviour is prevalent in fluid-particle flows due to high density ratios ($\rho_p \gg \rho_f$). This leads to the mean-feedback effect through drag - their primary coupling mechanism. Turbulence attenuation as a result of small heavy particles in the carrier flow is well established in the literature [15, 24, 26, 33, 50, 54, 57] and has been shown to be further influenced by the inhomogeneity of wall-bounded flow [53].

To date there have been numerous experimental studies investigating small heavy particles in wall-bounded, high Reynolds number flow [4, 9, 33, 50]. One valuable study is that of Fessler and Eaton [19] in which mean and turbulence statistics of dilute [14] fluid-particle flow were recorded in a vertically orientated backward-facing step. They report turbulence attenuation across three particle classifications (different Stokes number and mass loadings) and provide valuable insights into the particle behaviour in the free shear layer. Traditionally, the backward-facing step has been used as a benchmark for validation of single-phase turbulence models, as flow separation, reattachment and redevelopment are rife in engineering applications. Due to the complex nature of turbulence attenuation and the challenging physics in a backward-facing step configuration, its successful prediction has proven difficult [10, 36, 38, 51, 58].

There are two main approaches for predicting macroscale fluid-particle systems: the Eulerian-Lagrangian (E-L) method in which the fluid-phase is solved in an Eulerian frame and the particle-phase is solved with Lagrangian equations. Typically, all scales of motion are resolved except the boundary layers on the particle surfaces resulting in a high resolution of the flow field. It follows that E-L simulations are used for understanding fundamental phenomenon e.g. clustering [6, 49], and verifying experimental observations [25, 34]. Due to their expensive cost as each particle requires its own momentum equation, large particulate systems with high Reynolds number become inviable. This leads to the second approach: the Eulerian-Eulerian (E-E) methodology models both the fluid- and particle-phase as interpenetrating continua resulting in both phases acting as “fluids”. This reduces the computational cost considerably with the fully resolved scales of E-L being modelled. This approach then relies on constitutive relations to close the governing equations.

Numerous two-fluid (E-E) models have been derived using a one-step averaging

39 process [1, 13, 28, 47] e.g. volume- or time-averaging. Within this methodology,
 40 kinetic theory is used to close the particle-phase stress that appears in its momen-
 41 tum equation. This approach has been applied by many authors [2, 11, 12, 16, 27,
 42 40, 52, 60] with varying degrees of success. Recently, Fox [21] has shown that a
 43 two-step process is required in order to derive a Reynolds-Averaged multiphase tur-
 44 bulence model. In the aforementioned models, the multiphase models are derived
 45 analogously to a single-phase model using time- or volume-averaging techniques that
 46 can lead to ill-formed equations e.g. time averaging results in a diffusive term in the
 47 continuity equation.

48 In addition to this, a conceptual error has been highlighted. The statement
 49 $k_p = 3\langle\Theta\rangle_p$ is often found in these models which is inaccurate. This is due to the
 50 particle turbulent kinetic energy k_p , and the phase averaged (PA) granular tem-
 51 perature $\langle\Theta\rangle_p$, belonging to two different realisations of the flow. This distinction
 52 was first highlighted by Février et al. [20] in which particle velocities are decomposed
 53 into correlated k_p large-scale motion and uncorrelated $\langle\Theta\rangle_p$ small-scale motion. Both
 54 quantities are a result of separate models. It was shown that the correlated motion
 55 k_p arises due to the hydrodynamic (macroscale) model and the uncorrelated motion
 56 $\langle\Theta\rangle_p$ arises due to the kinetic (mesoscale) model.

57 The two-step derivation of Fox [21] has been shown to circumvent these issues.
 58 Beginning at the kinetic (mesoscale) equation [22], phase-space integration is applied
 59 to find the hydrodynamic (macroscale) moment equation which is then Reynolds-
 60 Averaged to form the Reynolds-Averaged Two-Fluid model (RA-TFM) after the ap-
 61 propriate closure modelling has been applied. This approach results in separate
 62 transport equations for the particle turbulence kinetic energy k_p and the PA gran-
 63 ular temperature $\langle\Theta\rangle_p$. Through the derivation of k_p the particle turbulent kinetic
 64 energy dissipation ε_p , is defined which appears as a source term in the transport
 65 equation of the PA granular temperature, $\langle\Theta\rangle_p$. This cascade of energy from corre-
 66 lated motion to uncorrelated motion is a crucial distinction. This leads to the particle
 67 fluctuation energy being written as $\kappa_p = k_p + 1.5\langle\Theta\rangle_p$. Février et al. [20] found that
 68 even for non-collisional flow, separate transport equations for k_p and $\langle\Theta\rangle_p$ were es-
 69 sential, a direct result of the energy cascade outlined previously. Given these recent
 70 advances in the field, the modelling of previously challenging turbulent fluid-particle
 71 interactions in the Eulerian-Eulerian framework become clearer and their successful
 72 prediction more likely.

73 The overarching motivation of the present work is to increase the current under-
 74 standing of the modelling of turbulent fluid-particle interaction in a complex flow
 75 field. We confine ourselves to turbulence attenuation of small heavy particles in
 76 a vertically orientated backward-facing step. The particles have material densities

77 much larger than the fluid ($\rho_p \gg \rho_f$) and diameters smaller than the Kolmogorov
78 length scale over the moderately dilute range $\mathcal{O}(10^{-4})$.

79 The RA-TFM of Fox [21] is implemented in OpenFOAM and applied to the
80 aforementioned flow configuration. The model predictions are compared against
81 benchmark experimental data of Fessler and Eaton [18, 19]. In addition, predictions
82 are also compared against the model of Peirano and Leckner [40] to highlight the
83 importance of separating correlated and uncorrelated motion. Analysis is carried
84 out on the mean particle stream-wise velocities and the fluctuation intensity of both
85 the particle and fluid phases. Applying the RA-TFM to wall-bounded flow requires
86 physical wall boundary conditions for the particle turbulent quantities, k_p , ε_p and
87 $\langle \Theta \rangle_p$. To this end the Johnson and Jackson [31] boundary conditions were recently
88 extended for the RA-TFM by Capecelatro et al. [8] and are implemented and applied
89 here to describe the particle-wall interaction.

90 The paper is organised as follows; in the following section the numerical model
91 is presented. This contains the RA-TFM in which the governing equations for each
92 phase are presented along with the fully coupled turbulence models. Next, the wall
93 boundary conditions used in this work are presented in their implemented form. Fol-
94 lowing this the numerical implementation of the RA-TFM into OpenFOAM is pro-
95 vided along with a description of the turbulence modelling implementation. Section
96 3 presents the results and discussion with the final section providing the conclusions.

97 **2. Numerical Model**

98 Here we begin by presenting the Reynolds-averaged transport equations from
 99 Fox [21]. The RA transport equations are presented in their conservative form with
 100 closures found in Table 5. For clarity the PA notation has been dropped and the PA
 101 variables along with their definitions can be found in Table 6. The particle phase
 102 continuity equation reads:

$$\frac{\partial \alpha_p \rho_p}{\partial t} + \nabla \cdot \alpha_p \rho_p \mathbf{u}_p = 0 \quad (1)$$

103 Where α_p is the volume fraction of particles, ρ_p is the density of the particles and
 104 \mathbf{u}_p is the particle phase velocity.

105 The momentum balance equation for the RA particulate phase is given as:

$$\begin{aligned} \frac{\partial \alpha_p \rho_p \mathbf{u}_p}{\partial t} + \nabla \cdot \alpha_p \rho_p \mathbf{u}_p \mathbf{u}_p = & \nabla \cdot 2(\mu_p + \mu_{pt}) \bar{\mathbf{S}}_p + \beta \left[(\mathbf{u}_f - \mathbf{u}_p) - \frac{\nu_{ft}}{\text{Sc}_{fs} \alpha_p \alpha_f} \nabla \alpha_p \right] \\ & - \nabla \left(p_p + \frac{2}{3} \alpha_p \rho_p k_p \right) - \alpha_p \nabla p_f + \alpha_p \rho_p \left[1 - C_p \alpha_f \left(1 - \frac{\rho_f}{\rho_p} \right) \right] \mathbf{g} \end{aligned} \quad (2)$$

106 Where the first term on the right hand side (RHS) contains the diffusive viscos-
 107 ity associated with the material viscosity and the particle turbulent viscosity. The
 108 forms for these are analogous to those of a fluid and can be found in Table 5. The
 109 second term is the momentum transfer term and contains both the slip velocity
 110 and a turbulent dispersion term. Through the denominator of the dispersion term
 111 $\text{Sc}_{fp} = (k_f/k_p)^{1/2}$ a Stokes number (St) dependency is introduced which accounts for
 112 dispersion for moderate to large St. The form of this equation enforces the correct
 113 behaviour, when there is a small St the particle turbulent kinetic energy $k_p \rightarrow k_f$
 114 thus returning 1; for a large St where k_p is small this represents a large value reducing
 115 the amount of dispersion i.e. the particles remain correlated with the fluid.

116 The third term is the pressure gradient along with the so-called turbulent pres-
 117 sure, with the fourth term being the covariance of the volume fraction and the fluid-
 118 pressure gradient. This term appears in both momentum equations and is typically
 119 assumed to be negligible. The last term contains the body forces (i.e. gravity)
 120 and the velocity-fluid-pressure-gradient covariance term. This term represents the
 121 correlations between the velocity and pressure gradients which arise from buoyancy.

122 The fluid phase continuity equation reads:

$$\frac{\partial \alpha_f \rho_f}{\partial t} + \nabla \cdot \alpha_f \rho_f \mathbf{u}_f = 0 \quad (3)$$

123 The momentum balance equation for the RA fluid phase is given as:

$$\begin{aligned} \frac{\partial \alpha_f \rho_f \mathbf{u}_f}{\partial t} + \nabla \cdot \alpha_f \rho_f \mathbf{u}_f \mathbf{u}_f &= \nabla \cdot 2(\mu_f + \mu_{ft}) \bar{\mathbf{S}}_f + \beta \left[(\mathbf{u}_p - \mathbf{u}_f) + \frac{\nu_{ft}}{Sc_{fs} \alpha_p \alpha_f} \nabla \alpha_p \right] \\ &\quad - \nabla \left(\alpha_f p_f + \frac{2}{3} \alpha_f \rho_f k_f \right) + \alpha_p \nabla p_f + \alpha_f \rho_f \left[1 + C_p \alpha_p \left(\frac{\rho_p}{\rho_f} - 1 \right) \right] \mathbf{g} \end{aligned} \quad (4)$$

124 The momentum equations are symmetric with opposite pressure gradients, hence the
125 corresponding term in the particle momentum equation (2) are defined in the same
126 manner but with respect the fluid phase.

127 The RA turbulent kinetic energy transport equation for the fluid-phase takes the
128 form:

$$\begin{aligned} \frac{\partial \alpha_f \rho_f k_f}{\partial t} + \nabla \cdot \alpha_f \rho_f k_f \mathbf{u}_f &= \nabla \cdot \left(\mu_t + \frac{\mu_{ft}}{\sigma_{fk}} \right) \nabla k_f + \alpha_f \rho_f \Pi_f - \alpha_f \rho_f \varepsilon_f \\ &\quad + 2\beta(k_{fp} - k_f) + \alpha_p \rho_p \Pi_{fp} + \alpha_p \rho_p \Pi_{\rho f} \end{aligned} \quad (5)$$

129 The first term on the RHS is the fluid-phase turbulent kinetic energy flux. The
130 second term Π_f represents kinetic energy production due to mean shear with the
131 third term being the turbulent kinetic energy dissipation. The remaining three terms
132 are the coupling terms: velocity correlations, mean slip and volume-fraction-velocity
133 correlations, respectively.

134 The RA turbulent kinetic energy dissipation transport equation for the fluid-
135 phase reads as:

$$\begin{aligned} \frac{\partial \alpha_f \rho_f \varepsilon_f}{\partial t} + \nabla \cdot \alpha_f \rho_f \varepsilon_f \mathbf{u}_f &= \nabla \cdot \left(\mu_t + \frac{\mu_{ft}}{\sigma_{fk}} \right) \nabla \varepsilon_f + \frac{\varepsilon_f}{k_f} \left[C_1 \alpha_f \Pi_f - C_2 \alpha_f \rho_f \varepsilon_f \right] \\ &\quad + 2C_3 \beta (\varepsilon_{fp} - \varepsilon_f) + C_4 \frac{\varepsilon_p}{k_p} \alpha_p \rho_p \Pi_{fp} + C_5 \frac{\varepsilon_p}{k_p} \alpha_p \rho_p \Pi_{\rho f} \end{aligned} \quad (6)$$

136 The first term on the RHS is the fluid-phase turbulent kinetic dissipation energy
137 flux. The second term Π_f is kinetic energy production due to mean shear with the
138 third term is dissipation. The remaining three terms are the coupling terms: velocity
139 correlations, mean slip and volume-fraction-velocity correlations, respectively. The
140 forms of these are as follows:

$$\Pi_f = 2\nu_{ft} \bar{\mathbf{S}}_f : \bar{\mathbf{S}}_f + \frac{2}{3} k_f \nabla \cdot \mathbf{u}_f \quad (7)$$

$$\Pi_{fp} = \left[C_g (\mathbf{u}_p - \mathbf{u}_f) - \frac{\nu_{ft}}{Sc_{fp} \alpha_p \alpha_f} \nabla \alpha_p \right] \cdot \left[\beta (\mathbf{u}_p - \mathbf{u}_f) + \frac{1}{\rho_p} \nabla p_f \right] \quad (8)$$

$$\Pi_{\rho f} = C_\rho \left(1 - \frac{\rho_f}{\rho_p}\right) \left[C_g \alpha_p \alpha_f (\mathbf{u}_p - \mathbf{u}_f) - \frac{\nu_{ft}}{S C_{fp}} \nabla \alpha_p \right] \cdot \mathbf{g} \quad (9)$$

141 Where Π_f is the production of the turbulent kinetic energy, Π_{fp} is due to mean
 142 slip and $\Pi_{\rho f}$ is due to volume-fraction-velocity correlations. The coupling terms take
 143 the form of $k_{fp} = \beta_k \sqrt{k_f k_p}$ and $\varepsilon_{fp} = \beta_\varepsilon \sqrt{\varepsilon_f \varepsilon_p}$. Where correlation coefficients are
 144 $0 < \beta_k, \beta_\varepsilon \leq 1$. These terms represent the fluid-velocity covariance and their exact
 145 closure is still uncertain, a detailed discussion on this point can be found in [21].
 146 This form is adopted as it shows correct limiting behaviour for large St as well as
 147 diminishing correctly in the absence of the particulate phase.

148 The RA particle-phase turbulent kinetic energy reads as:

$$\begin{aligned} \frac{\partial \alpha_p \rho_p k_p}{\partial t} + \nabla \cdot \alpha_p \rho_p k_p \mathbf{u}_p = \nabla \cdot \left(\mu_p + \frac{\mu_{pt}}{\sigma_{pk}} \right) \nabla k_p + \alpha_p \rho_p \Pi_p - \alpha_p \rho_p \varepsilon_p \\ + 2\beta(k_{fp} - k_p) + \alpha_p \rho_p \Pi_{\rho p} \end{aligned} \quad (10)$$

149 The first term on the RHS is the particle-phase turbulent kinetic energy flux. The
 150 second term Π_p is kinetic energy production due to mean shear with the third term
 151 being the particle turbulent kinetic energy dissipation. The remaining two terms
 152 are the coupling terms: velocity correlations, and the combination of the buoyancy
 153 induced and mean slip terms.

154 The RA particle-phase turbulent kinetic energy dissipation transport equation reads:

$$\begin{aligned} \frac{\partial \alpha_p \rho_p \varepsilon_p}{\partial t} + \nabla \cdot \alpha_p \rho_p \varepsilon_p \mathbf{u}_p = \nabla \cdot \left(\mu_p + \frac{\mu_{pt}}{\sigma_{pk}} \right) \nabla \varepsilon_p + \frac{\varepsilon_p}{k_p} (C_1 \alpha_p \rho_p \Pi_p - C_2 \alpha_p \rho_p \varepsilon_p) \\ + 2C_3 \beta (\varepsilon_{fp} - \varepsilon_p) + C_5 \frac{\varepsilon_p}{k_p} \alpha_p \rho_p \Pi_{\rho p} \end{aligned} \quad (11)$$

155 The first term on the RHS is the particle phase turbulent kinetic dissipation
 156 energy flux. The second term Π_p is kinetic energy production due to mean shear
 157 with the third term being its dissipation. The remaining two terms are the coupling
 158 terms: velocity correlations, and the combination of the buoyancy induced and mean
 159 slip terms. The second term contains, Π_p which is the production of the turbulent
 160 kinetic energy and is expressed as:

$$\Pi_p = 2\nu_{pt} \bar{\mathbf{S}}_p : \bar{\mathbf{S}}_p + \frac{2}{3} k_p \nabla \cdot \mathbf{u}_p \quad (12)$$

161 It should be noted here that the final term on the RHS is a compressive term
 162 that appears in compressible turbulence modelling and plays a similar role of the bulk
 163 viscosity found in the typical granular temperature formulations in the literature [40],

164 [51]. Finally, the buoyancy-induced source term $\Pi_{\rho f}$ is added to the mean slip Π_{fp}
 165 to be reformulated as $\Pi_{\rho p}$ which is read as:

$$\Pi_{\rho p} = C_\rho C_p \alpha_f \left(1 - \frac{\rho_f}{\rho_p}\right) (\mathbf{u}_p - \mathbf{u}_f) \cdot \mathbf{g} \quad (13)$$

166 The granular temperature equation reads as:

$$\frac{3}{2} \left[\frac{\partial \alpha_p \rho_p \Theta_p}{\partial t} + \nabla \cdot \alpha_p \rho_p \Theta_p \mathbf{u}_p \right] = \nabla \cdot \left(\kappa_\Theta + \frac{3\mu_{pt}}{2Pr_{pt}} \right) \nabla \Theta_p + 2\mu_p \bar{\mathbf{S}}_p : \bar{\mathbf{S}}_p \quad (14)$$

$$- p_p \nabla \cdot \mathbf{u}_p + \alpha_p \rho_p \varepsilon_p - 3\beta \Theta_p - \gamma$$

167 The first term on the RHS is the PA granular temperature flux which is made up
 168 of two contributions, the granular temperature flux and the turbulent granular flux.
 169 The former is the granular conductivity of which there are various formulations in the
 170 literature. Here the formulation of Syamlal and O'Brien [48] is used as it correctly
 171 tends to zero in the dilute limit [51]. The latter term is the turbulent flux and
 172 includes the particle turbulent viscosity. The second term is a laminar source term
 173 due to viscous stresses. The third term is a pressure dilation term which accounts
 174 for compressibility. The fourth term is of particular interest as it represents the
 175 turbulent particle kinetic energy dissipation which appears here as a positive source
 176 term. The physical interpretation of this means that as large scale particle turbulent
 177 kinetic energy is dissipated, small scale granular temperature is produced. The two
 178 remaining terms represent decrease of granular temperature due to drag and decrease
 179 of granular temperature due to inelastic collisions.

Table 1: Turbulence model parameters.

C_p	C_g	C_ρ	C_1	C_2	C_3	C_4	C_5	β_k	β_ε	$C_{f\mu}$	$C_{p\mu}$
1	0	1	1.44	1.92	1	1	1	1	1	0.09	0.09

180 The full form of the equations have been presented here with no mention of their
 181 relevance to the flow regime being simulated in this work. As the density ratio is
 182 high the buoyancy induced terms are negligible. The coefficient $C_g \rightarrow 0$ due to
 183 the small mass loading used in this work, a more thorough discussion on this topic
 184 can be found in [6, 7, 21]. The buoyancy terms were indeed found to be negligible
 185 but are retained here to show their solution treatment. Similarly, the compressible
 186 turbulence correction terms depend on the particle-phase Mach number, which is
 187 expected to be large for large St. Given the St values used in this study this is not

188 expected to be the case but have been retained. A thorough discussion on this topic
 189 is provided in Section 3.4.1.

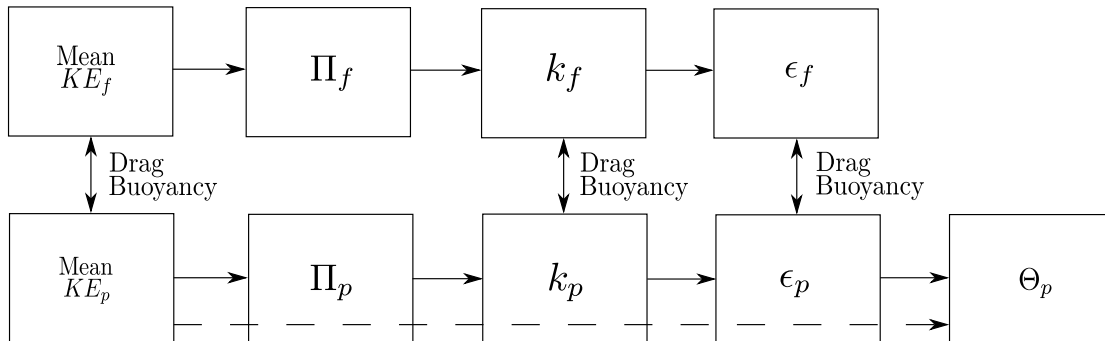


Figure 1: Schematic showing the energy cascade between each variable within the multiphase model [21]. The interaction between each quantity is shown along with their respective energy transfer mechanisms. The dashed line represents the energy flow in the (mesoscale) laminar model.

190 Fig. 1 shows an overall picture of the RA-TFM. As can be seen the energy cascade
 191 is almost identical in both phases. Starting with the mean particle kinetic energy
 192 $\frac{1}{2}\mathbf{u}_p \cdot \mathbf{u}_p$, the energy transfer to the turbulent particle kinetic energy is given by the
 193 production term which is Π_p i.e. the shear. This then generates k_p and is dissipated
 194 by the turbulent kinetic energy dissipation equation. Finally, this dissipation term
 195 ε_p appears in the granular temperature Θ_p as a positive source term, meaning that
 196 as the particle turbulent kinetic energy dissipates, granular energy is produced. As
 197 can be seen both turbulent quantities interact via drag and buoyancy terms in the
 198 same way the governing equations do. If there is dissipation due to collisions then
 199 the granular temperature is reduced due to particle heating.

200 *2.1. Particle wall boundary conditions*

201 The wall boundary conditions for the particle phase require additional modelling.
 202 Recently, Capecelatro et al. [8] started from the Johnson and Jackson [31] wall bound-
 203 ary conditions and derived wall boundary conditions for the particle turbulence quan-
 204 tities k_p , ε_p and Θ_p . Here we present the boundary conditions in their implemented
 205 form applicable for Finite-Volume-Method codes and begin with the wall boundary
 206 condition for the particle velocity \mathbf{u}_p .

$$\mathbf{n} \cdot \bar{\boldsymbol{\sigma}}_p \nabla \mathbf{u}_{p,w} = -\frac{\pi}{6} \frac{\alpha_p}{\alpha_{p,max}} \phi \rho_p g_0 \sqrt{3\Theta_p} \mathbf{u}_{p,w} \quad (15)$$

207 Here we define $\mathbf{u}_{p,w}$ as the particle slip velocity parallel to the wall, $\mathbf{u}_{p,w} = \mathbf{u}_p - \mathbf{u}_w$
 208 with \mathbf{u}_w defined as the wall velocity. Where $\bar{\boldsymbol{\sigma}}_p$ is the particle viscous stress tensor
 209 and we denote \mathbf{n} as the unit vector normal to the wall. Then equation 15 is recast
 210 into a more compact form

$$\mathbf{n} \cdot \bar{\boldsymbol{\sigma}}_p \nabla \mathbf{u}_{p,w} = -\mathcal{D}_w \mathbf{u}_{p,w} \quad (16)$$

211 where the term $\mathcal{D}_w = \phi \mathcal{V}_w$ representing ϕ , the specularity coefficient and the term
 212 $\mathcal{V}_w = \frac{\pi}{6} \frac{\alpha_p}{\alpha_{p,max}} \rho_p \sqrt{3\Theta_p} g_0$ which contains the tangential momentum $\frac{\pi}{6} \frac{\alpha_p}{\alpha_{p,max}} \rho_p$ (omit-
 213 ting the particle slip velocity parallel to the wall $\mathbf{u}_{p,w}$) and the collisional frequency
 214 $\sqrt{3\Theta_p} g_0$. This boundary condition prescribes a particle partial-slip velocity at the
 215 wall. From this condition it follows that the components of the Reynolds stress tensor
 216 $\langle \mathbf{u}_p'' \mathbf{u}_p'' \rangle_p$ need not be zero at the wall unlike in the fluid phase. As we are interested
 217 in modelling the particle-wall interaction of the particle turbulent kinetic energy k_p
 218 we assume isotropy in the fluctuating components.

$$k_p = \frac{1}{2} (\mathbf{u}_{p,x}''^2 + \mathbf{u}_{p,y}''^2 + \mathbf{u}_{p,z}''^2) \quad (17)$$

219 Equating the principal Reynolds stress components ($\mathbf{u}_{p,x}''^2 \equiv \mathbf{u}_{p,y}''^2 \equiv \mathbf{u}_{p,z}''^2$) one
 220 arrives at $k_p = 1.5 \mathbf{u}_p''^2$ and substituting into Equation 16 by employing the PA
 221 decomposition (see Table 6) the wall boundary condition for k_p reads

$$\mathbf{n} \cdot \bar{\boldsymbol{\sigma}}_p \nabla k_p = -2\mathcal{D}_w k_p \quad (18)$$

222 Following on from this a condition for the particle turbulent kinetic energy dissi-
 223 pation rate ε_p can be prescribed:

$$\mathbf{n} \cdot \bar{\boldsymbol{\sigma}}_p \nabla \varepsilon_p = -2\mathcal{D}_w \varepsilon_p \quad (19)$$

224 Finally, the wall boundary condition for the granular temperature can be found
 225 by Reynolds averaging the Johnson and Jackson [31] which reads as

$$\mathbf{n} \cdot \mathbf{q}_\Theta \frac{3}{2} = \phi \mathcal{D}_w |\mathbf{u}_{p,w}|^2 - \frac{3}{2} \mathcal{D}_\kappa \Theta_p \quad (20)$$

226 where \mathbf{q}_Θ is the granular temperature flux and with $\mathcal{D}_\kappa = (1 - e_w)^2 \mathcal{D}_w$ and e_w
 227 is the restitution of coefficient with the wall. It follows from this that this term
 228 represents the energy loss through particle collisions with the wall. The first term
 229 on the RHS represents the increase of the granular temperature due to the relative
 230 velocity with the wall. This means that the slip condition at the wall is capable of
 231 increasing the granular temperature. The particle-wall coefficient, e_w was set equal
 232 to 0.9. The specularity coefficient used throughout was, $\phi = 0.001$ and the influence
 233 of this parameter is discussed in Section 3.3.4.

234 *2.2. Numerical implementation*

235 Here we follow the phase intensive formulation of Rusche [43], Weller [55]. We
 236 rewrite the equations in their non-conservative form by expanding both the convec-
 237 tive term and dividing by density and volume fraction.

238 Additionally, the phase respective Reynolds stress tensor is formulated by group-
 239 ing the kinematic and turbulent viscosity into an effective viscosity, $\nu_{\text{eff},i} = \nu_i + \nu_{it}$
 240 and employing the Boussinesq hypothesis. Now, we can write the Reynolds stress
 241 tensor in the form:

$$\bar{\mathbf{R}}_{\text{eff},p} = -2\nu_{\text{eff},p}\bar{\mathbf{S}}_p + \frac{2}{3}\nu_{\text{eff},p}\mathbf{I}\nabla \cdot \mathbf{u}_p + \frac{2}{3}\mathbf{I}k_p \quad (21)$$

$$\bar{\mathbf{R}}_{\text{eff},f} = -2\nu_{\text{eff},f}\bar{\mathbf{S}}_f + \frac{2}{3}\nu_{\text{eff},f}\mathbf{I}\nabla \cdot \mathbf{u}_f + \frac{2}{3}\mathbf{I}k_f \quad (22)$$

242 For simplicity the turbulent dispersion term is now denoted as \mathcal{D} , separating the
 243 drag contributions into explicit and implicit terms and dividing by both the phase
 244 fraction and density we are left with:

$$\begin{aligned} \frac{\partial \mathbf{u}_p}{\partial t} + \nabla \cdot (\mathbf{u}_p \mathbf{u}_p) - \mathbf{u}_p \nabla \cdot \mathbf{u}_p + \frac{\nabla \alpha_p}{\alpha_p + \delta} \cdot \bar{\mathbf{R}}_{\text{eff},p}^c + \nabla \cdot \bar{\mathbf{R}}_{\text{eff},p}^c - \nabla \cdot (\nu_{\text{eff},p} \nabla \mathbf{u}_p) + \frac{\beta \mathbf{u}_p}{\alpha_p \rho_p} \\ - \nabla \cdot \left(\nu_{\text{eff},p} \frac{\nabla \alpha_p}{\alpha_p + \delta} \mathbf{u}_p \right) + \mathbf{u}_p \nabla \cdot \left(\nu_{\text{eff},p} \frac{\nabla \alpha_p}{\alpha_p + \delta} \right) \\ = \frac{\beta \mathbf{u}_f}{\alpha_p \rho_p} - \frac{\beta \mathcal{D} \nabla \alpha_p}{\alpha_p \rho_p} - \frac{\nabla p_p}{\alpha_p \rho_p} - \frac{\nabla p_f}{\rho_p} + \mathbf{g} - \alpha_f \left(1 - \frac{\rho_f}{\rho_p} \right) \mathbf{g} \end{aligned} \quad (23)$$

$$\begin{aligned} \frac{\partial \mathbf{u}_f}{\partial t} + \nabla \cdot (\mathbf{u}_f \mathbf{u}_f) - \mathbf{u}_f \nabla \cdot \mathbf{u}_f + \frac{\nabla \alpha_f}{\alpha_f + \delta} \cdot \bar{\mathbf{R}}_{\text{eff},f}^c + \nabla \cdot \bar{\mathbf{R}}_{\text{eff},f}^c - \nabla \cdot (\nu_{\text{eff},f} \nabla \mathbf{u}_f) + \frac{\beta \mathbf{u}_f}{\alpha_f \rho_f} \\ - \nabla \cdot \left(\nu_{\text{eff},f} \frac{\nabla \alpha_f}{\alpha_f + \delta} \mathbf{u}_f \right) + \mathbf{u}_f \nabla \cdot \left(\nu_{\text{eff},f} \frac{\nabla \alpha_f}{\alpha_f + \delta} \right) \\ = \frac{\beta \mathbf{u}_p}{\alpha_f \rho_f} + \frac{\beta \mathcal{D} \nabla \alpha_p}{\alpha_f \rho_f} - \frac{\nabla p_f}{\rho_f} - \frac{\alpha_p \nabla p_f}{\alpha_f \rho_f} + \mathbf{g} + \alpha_p \left(\frac{\rho_p}{\rho_f} - 1 \right) \mathbf{g} \end{aligned} \quad (24)$$

245 where δ is introduced to avoid a division by zero. As it can be seen from the system
 246 of equations in Eqs. 2 & 4 no diffusive flux exists that can be treated implicitly. This
 247 can have advantages when solving the equations i.e enhanced matrix positively and
 248 diagonal dominance. Therefore, following Weller [55], Rusche [43] the Reynolds stress
 249 term can be rewritten into a diffusive and corrective component:

$$\begin{aligned}
\bar{\mathbf{R}}_{\text{eff},i} &= \bar{\mathbf{R}}_{\text{eff},i} + \nu_{\text{eff},i} \nabla \mathbf{u}_i - \nu_{\text{eff},i} \nabla \mathbf{u}_i \\
&= -\nu_{\text{eff},i} (\nabla \mathbf{u}_i + \nabla^T \mathbf{u}_i) + \frac{2}{3} \nu_{\text{eff},i} \mathbf{I} \nabla \cdot \mathbf{u}_i \\
&\quad + \frac{2}{3} \mathbf{I} k_i + \nu_{\text{eff},i} \nabla \mathbf{u}_i - \nu_{\text{eff},i} \nabla \mathbf{u}_i \\
&= (-\nu_{\text{eff},i} \nabla^T \mathbf{u}_i + \frac{2}{3} \nu_{\text{eff},i} \mathbf{I} \nabla \cdot \mathbf{u}_i + \frac{2}{3} k_i \mathbf{I}) - \nu_{\text{eff},i} \nabla \mathbf{u}_i \\
&= \bar{\mathbf{R}}_{\text{eff},i}^c - \nu_{\text{eff},i} \nabla \mathbf{u}_i
\end{aligned} \tag{25}$$

250 It is important to clarify the behaviour of terms with the volume fraction in their
251 denominator. For the first contribution due to drag i.e. the third term on the RHS
252 the coefficient β contains $\alpha_p \alpha_f$ which ensures the correct behavior of the function
253 as $\alpha_p \rightarrow 0$. The second term containing turbulent dispersion contains the gradient
254 of volume fraction which in the limit $\alpha_p \rightarrow 0$ means that the ratio approaches zero.
255 Finally, the fluid velocity-pressure-covariance term contains the volume fraction in
256 its denominator, however due to the particle packing limit ensured by the particle's
257 structural properties the volume fraction of the fluid phase does not approach 0.

258 2.3. Discretisation of the intensive momentum equations

259 First, we discretise the left hand side of the equation which contains the convective
260 and diffusive transport terms.

$$\begin{aligned}
\mathcal{T}_p &:= \left[\frac{\partial \mathbf{u}_p}{\partial t} \right] + \left[\nabla \cdot (\mathbf{u}_p [\mathbf{u}_p]) \right] - \left[(\nabla \cdot \mathbf{u}_p) [\mathbf{u}_p] \right] + \frac{\nabla \alpha_p}{\alpha_p + \delta} \cdot \bar{\mathbf{R}}_{\text{eff},p}^c + \nabla \cdot \bar{\mathbf{R}}_{\text{eff},p}^c \\
&\quad - \left[\nabla \cdot (\nu_{\text{eff},p} \nabla [\mathbf{u}_p]) \right] - \left[\nabla \cdot (\nu_{\text{eff},p} \frac{\nabla \alpha_p}{\alpha_p + \delta} [\mathbf{u}_p]) \right] \\
&\quad - \left[\nabla \cdot (\nu_{\text{eff},p} \frac{\nabla \alpha_p}{\alpha_p + \delta}) [\mathbf{u}_p] \right] + \left[\frac{\beta \mathbf{u}_p}{\alpha_p \rho_p} \right]
\end{aligned} \tag{26}$$

$$\begin{aligned}
\mathcal{T}_f &:= \left[\frac{\partial \mathbf{u}_f}{\partial t} \right] + \left[\nabla \cdot (\mathbf{u}_f [\mathbf{u}_f]) \right] - \left[(\nabla \cdot \mathbf{u}_f) [\mathbf{u}_f] \right] + \frac{\nabla \alpha_f}{\alpha_f + \delta} \cdot \bar{\mathbf{R}}_{\text{eff},f}^c + \nabla \cdot \bar{\mathbf{R}}_{\text{eff},f}^c \\
&\quad - \left[\nabla \cdot (\nu_{\text{eff},f} \nabla [\mathbf{u}_f]) \right] - \left[\nabla \cdot (\nu_{\text{eff},f} \frac{\nabla \alpha_f}{\alpha_f + \delta} [\mathbf{u}_f]) \right] \\
&\quad - \left[\nabla \cdot (\nu_{\text{eff},f} \frac{\nabla \alpha_f}{\alpha_f + \delta}) [\mathbf{u}_f] \right] + \left[\frac{\beta \mathbf{u}_f}{\alpha_f \rho_f} \right]
\end{aligned} \tag{27}$$

261 where $[\cdot]$ is the implicit discretisation of the term, \mathcal{T}_p & \mathcal{T}_f represents the numer-
262 ical coefficients of each respective algebraic system given by the discretisation. The

263 second and third terms on the RHS represent convection and have been split up
 264 into a convection term minus a divergence terms as it enhances boundedness of the
 265 solution.

266 \mathcal{T}_p & \mathcal{T}_f represents the system of algebraic equations from the discretised Eqs.
 267 26 & 27 which appear in the form,

$$(\mathcal{T}_p)_{coeffs} \mathbf{u}_p = (\mathcal{T}_p)_s \quad (28a)$$

$$(\mathcal{T}_f)_{coeffs} \mathbf{u}_f = (\mathcal{T}_f)_s \quad (28b)$$

268 This discretised form of the momentum equations will be revisited once the source
 269 terms on the RHS are addressed.

270 Now addressing the RHS of Eq. 23 & 24 which reads as

$$\dots = \frac{\beta \mathbf{u}_f}{\alpha_p \rho_p} - \frac{\beta \mathcal{D} \nabla \alpha_p}{\alpha_p \rho_p} - \frac{\nabla p_p}{\alpha_p \rho_p} - \frac{\nabla p_f}{\rho_p} + \mathbf{g} - \alpha_f \left(1 - \frac{\rho_f}{\rho_p}\right) \mathbf{g} \quad (29a)$$

$$\dots = \frac{\beta \mathbf{u}_p}{\alpha_f \rho_f} + \frac{\beta \mathcal{D} \nabla \alpha_p}{\alpha_f \rho_f} - \frac{\nabla p_f}{\rho_f} - \frac{\alpha_p \nabla p_f}{\alpha_f \rho_f} + \mathbf{g} + \alpha_p \left(\frac{\rho_p}{\rho_f} - 1\right) \mathbf{g} \quad (29b)$$

271 denoting the buoyancy terms to be $\mathbf{g}_p^* = \mathbf{g}(1 - \alpha_p(1 - \frac{\rho_f}{\rho_p}))$ & $\mathbf{g}_f^* = \mathbf{g}(1 + \alpha_p(\frac{\rho_p}{\rho_f} - 1))$
 272 we can write

$$\dots = \frac{\beta \mathbf{u}_f}{\alpha_p \rho_p} - \frac{\beta \mathcal{D} \nabla \alpha_p}{\alpha_p \rho_p} - \frac{\nabla p_f}{\rho_p} - \frac{\nabla p_p}{\alpha_p \rho_p} + \mathbf{g}_p^* \quad (30a)$$

$$\dots = \frac{\beta \mathbf{u}_p}{\alpha_f \rho_f} + \frac{\beta \mathcal{D} \nabla \alpha_p}{\alpha_f \rho_f} - \frac{\nabla p_f}{\rho_f} - \frac{\alpha_p \nabla p_f}{\alpha_f \rho_f} + \mathbf{g}_f^* \quad (30b)$$

273 Following the solution procedure of Weller [55] all terms on the RHS are evaluated
 274 at cell faces. In order to avoid checker-boarding in the solution, which is a prevalent
 275 problem on collocated grids due to the storage of values at cell centres and interpo-
 276 lating onto the face, the group of terms on the RHS are treated in a Rhie-Chow like
 277 manner Rhie and Chow [42].

278 2.4. Phase momentum flux correction equations

279 Now a semi-discretised formulation of both the particle- and fluid-phase can be
 280 written. Invoking Eqs. 28 and splitting up the total coefficients appearing in each
 281 system into diagonal and explicit \mathbf{H} [30] coefficients. The latter consisting of two
 282 parts, the neighbouring coefficients (multiplied by its respective phase velocity) and
 283 the source terms, $\mathbf{H}_i = -(\mathbf{A}_i)_N \mathbf{u}_i + (\mathbf{A}_i)_S$. The equations can then be written as:

$$\mathbf{A}_p \mathbf{u}_p = \mathbf{H}_p + \frac{\beta \mathbf{u}_f}{\alpha_p \rho_p} - \frac{\beta \mathcal{D} \nabla \alpha_p}{\alpha_p \rho_p} - \frac{\nabla p_f}{\rho_p} - \phi_{p,p} + \mathbf{g}_p^* \quad (31a)$$

$$\mathbf{A}_f \mathbf{u}_f = \mathbf{H}_f + \frac{\beta \mathbf{u}_p}{\alpha_f \rho_f} + \frac{\beta \mathcal{D} \nabla \alpha_p}{\alpha_f \rho_f} - \frac{\nabla p_f}{\rho_f} - \phi_{f,g} + \mathbf{g}_f^* \quad (31b)$$

284 Rearranging Eqs. 31 gives the phase momentum correction equations, note these
 285 equations are not used in the solution algorithm, but are required to derive a flux
 286 predictor and corrector:

$$\mathbf{u}_p = \frac{\mathbf{H}_p}{\mathbf{A}_p} + \frac{\beta \mathbf{u}_f}{\alpha_p \rho_p \mathbf{A}_p} - \frac{\beta \mathcal{D} \nabla \alpha_p}{\alpha_p \rho_p \mathbf{A}_p} - \frac{\nabla p_f}{\rho_p \mathbf{A}_p} - \frac{\phi_{p,p}}{\mathbf{A}_p} + \frac{\mathbf{g}_p^*}{\mathbf{A}_p} \quad (32a)$$

$$\mathbf{u}_f = \frac{\mathbf{H}_f}{\mathbf{A}_f} + \frac{\beta \mathbf{u}_p}{\alpha_f \rho_f \mathbf{A}_f} + \frac{\beta \mathcal{D} \nabla \alpha_p}{\alpha_f \rho_f \mathbf{A}_f} - \frac{\nabla p_f}{\rho_f \mathbf{A}_f} - \frac{\phi_{f,g}}{\mathbf{A}_f} + \frac{\mathbf{g}_f^*}{\mathbf{A}_f} \quad (32b)$$

287 2.5. Construction of the pressure equation

288 In order to derive a pressure equation the continuity equation is enforced globally.
 289 The global continuity equation thus reads:

$$\nabla \cdot [(\alpha_p)_f \phi_p + (\alpha_f)_f \phi_f] = 0 \quad (33)$$

290 where the subscript $(\)_f$ denotes the face value and $\phi_i = (\mathbf{u}_i)_f \cdot \mathbf{S}_f$ is the volumetric
 291 face flux i.e. the sum of all the fluxes over a control volume. From here the phase
 292 fluxes for each phase are found by interpolating the momentum correction equation
 293 (Eqs. 32) onto face centres. Using central differencing, we can write

$$\phi_p = \phi_p^* - \left(\frac{1}{\rho_p \mathbf{A}_p} \right)_f \nabla_f^\perp p_f \cdot \mathbf{S}_f \quad (34a)$$

$$\phi_f = \phi_f^* - \left(\frac{1}{\rho_f \mathbf{A}_f} \right)_f \nabla_f^\perp p_f \cdot \mathbf{S}_f \quad (34b)$$

294 where the flux predictions ϕ_p^* & ϕ_f^* are given by

$$\begin{aligned} \phi_p^* = & \left(\frac{\mathbf{H}_p}{\mathbf{A}_p} \right)_f \cdot \mathbf{S}_f + \left(\frac{\beta}{\alpha_p \rho_p \mathbf{A}_p} \right)_f \phi_f - \left(\frac{\beta \mathcal{D}}{\alpha_p \rho_p \mathbf{A}_p} \right)_f \nabla_f^\perp \alpha_p \cdot \mathbf{S}_f \\ & - \left(\frac{1}{\mathbf{A}_p} \right)_f \nabla_f^\perp p_p \cdot \mathbf{S}_f + \left(\frac{1}{\mathbf{A}_p} \right)_f \mathbf{g}_p^* \cdot \mathbf{S}_f \end{aligned} \quad (35)$$

$$\begin{aligned} \phi_f^* = & \left(\frac{\mathbf{H}_f}{\mathbf{A}_f} \right)_f \cdot \mathbf{S}_f + \left(\frac{\beta}{\alpha_f \rho_f \mathbf{A}_f} \right)_f \phi_p - \left(\frac{\beta \mathcal{D}}{\alpha_f \rho_f \mathbf{A}_f} \right)_f \nabla_f^\perp \alpha_p \cdot \mathbf{S}_f \\ & - \left(\frac{\alpha_p}{\alpha_f \rho_f \mathbf{A}_f} \right)_f \nabla_f^\perp p_f \cdot \mathbf{S}_f + \left(\frac{1}{\mathbf{A}_f} \right)_f \mathbf{g}_f^* \cdot \mathbf{S}_f \end{aligned} \quad (36)$$

295 Now the pressure equation can be constructed by substituting Eq. 34 into Eq.
296 33 which reads:

$$\left[\nabla \cdot \left(D_p \nabla_f^\perp [p_f] \cdot \mathbf{S}_f \right) \right] = \nabla \cdot \left((\alpha_p)_f \phi_p^* + (\alpha_f)_f \phi_f^* \right) \quad (37)$$

297 where

$$D_p = \left(\frac{\alpha_p}{\rho_p \mathbf{A}_p} + \frac{\alpha_f}{\rho_f \mathbf{A}_f} \right)_f, \quad (38)$$

298 and the pressure gradient has been discretised implicitly on the LHS as a diffusion
299 term i.e. Laplacian. Essentially a shared or mixture pressure field is solved for, this
300 ensures that continuity is obeyed throughout as the coupling is provided through the
301 pressure equation. Once this equation has been solved the phase fluxes need to be
302 updated to satisfy continuity, as in the predictor step the influence of the pressure
303 gradient is removed, this can be achieved by invoking Eq. 34. From this stage the
304 solution does not completely satisfy continuity as the velocities, which are stored at
305 the cell centres, need to be updated with the influence of the pressure gradient.

This is achieved by invoking:

$$\mathbf{u}_p = \frac{\mathbf{H}_p}{\mathbf{A}_p} + \left[\phi_p^* - \left(\frac{1}{\rho_p \mathbf{A}_p} \right)_f \nabla_f^\perp p_f \cdot \mathbf{S}_f \right]_{f \rightarrow c} \quad (39a)$$

$$\mathbf{u}_f = \frac{\mathbf{H}_f}{\mathbf{A}_f} + \left[\phi_f^* - \left(\frac{1}{\rho_f \mathbf{A}_f} \right)_f \nabla_f^\perp p_f \cdot \mathbf{S}_f \right]_{f \rightarrow c} \quad (39b)$$

306 where the subscript $f \rightarrow c$ denotes a vector field reconstruction from face flux
307 values to cell centre values. The influence of the gradient of pressure is incorporated
308 into the reconstruction of the phase velocity - this ensures the phase velocity obeys
309 continuity. Once this is completed the PISO loop is complete.

310 2.6. Solution of the phase-mixed continuity equation

311 In practice the phase-mixed continuity equation is solved first based on the initial
312 conditions but for the sake of logical progression is presented now. Following Weller

313 [55] the particle phase continuity equation ?? can be reformulated as:

$$\frac{\partial \alpha_p}{\partial t} + \nabla \cdot (\mathbf{u}_T \alpha_p) + \nabla \cdot (\mathbf{u}_r \alpha_p \alpha_f) = 0 \quad (40)$$

314 where $\mathbf{u}_T = \alpha_p \mathbf{u}_p + \alpha_f \mathbf{u}_f$ is the mixture velocity and $\mathbf{u}_r = \mathbf{u}_p - \mathbf{u}_f$ is the relative
315 velocity. This equation can then be discretised as

$$\left[\frac{\partial [\alpha_p]}{\partial t} \right] + \left[\nabla \cdot (\phi [\alpha_p]_f) \right] + \left[\nabla \cdot (\phi_{r,p} [\alpha_p]_f) \right] = 0 \quad (41)$$

316 where $\phi_{r,p} = (\alpha_f)_f \phi_r$ and $\phi_r = \phi_p - \phi_f$.

317 The second term on the LHS is ensured to be bounded between 0 and 1 due to the
318 mixture flux, $\phi = (\mathbf{u}_p)_f \cdot \mathbf{S}_f + (\mathbf{u}_f)_f \cdot \mathbf{S}_f$ satisfying the mixture continuity equation.
319 The third term is bounded by employing ϕ_r in the convective scheme by interpolating
320 α_p to the face and $-\phi_r$ in the face interpolation of α_f . This system is solved using
321 the the Multi-dimensional Universal Limiter with Explicit Solution (MULES) [59]
322 which is a flux-corrected transport algorithm which enhances robustness, stability
323 and convergence.

The numerical procedure adopted in the segregated algorithm:

1. Solve the volume fraction (Eq. 41).
2. Construct \mathbf{A}_i in each phase (Eqs. 28).
3. Enter PISO-Loop:
 - 324 (a) Predict fluxes using Eqs. 35 & 36.
 - (b) Construct and solve the pressure equation (Eq. 37).
 - (c) Correct the phase fluxes using Eqs. 34.
 - (d) Reconstruct the phase velocities using Eqs. 39.
4. Solve the system of phase energy equations

325 The $k_p - \varepsilon_p$ transport equation is implemented in a similar manner to the $k_f - \varepsilon_f$
326 transport equation. A thorough discussion of its implementation in OpenFOAM can
327 be found in [37, 30, 43]. The coupling terms found in each equation are handled in a
328 segregated manner due to the velocity-pressure solution treatment. From the solution
329 of the aforementioned transport equations the granular temperature is then solved
330 as the particle turbulence dissipation ε_p appears as a source term in the transport
331 equation of granular temperature Θ_p .

332 *2.7. Numerical solution*

333 The open-source toolbox OpenFOAM [56] is used to solve the RA-TFM equa-
334 tions. To handle the pressure-velocity coupling the Pressure Implicit with Splitting
335 Operators (PISO) algorithm [17, 29] is used. The volume fraction is solved using a
336 Multi-dimensional Universal Limiter with Explicit Solution (MULES) [59] which is
337 a flux-corrected transport algorithm which ensures robustness, stability and conver-
338 gence.

339 *2.8. Simulation cases*

340 The computational domain is a two-dimensional channel section as seen in Fig.
 341 2 which starts at $60h$ upstream of the step to allow the flow to fully develop and
 342 extends $30H$ downstream. The material constants for each respective case can be
 343 found in Table 2. As reported in the experiments the centreline velocity, U_0 is 10.5
 344 ms^{-1} at the step ($x/H = 0$) and this corresponded to an inlet value of 9.3ms^{-1} . Mass
 345 loading is given by a uniform particle volume fraction across the inlet, this is achieved
 346 by assuming a constant particle-to-fluid velocity ratio. Wall functions for the fluid
 347 phase are used throughout and the effect of the particles on the boundary layer is
 348 not considered here. For the particle phase the boundary conditions described in
 349 Section 2.1 are used for the turbulent quantities. At the inlet a first estimate of the
 350 two turbulent quantities is determined as follows; $k_p = 1/3k_f$ and $\varepsilon_p = 1/3\varepsilon_f$ (for
 351 a more elaborate approach see [21]). For the granular temperature a small value is
 352 specified; $\Theta_p = 1.0 \times 10^{-8} \text{m}^2 \text{s}^{-2}$ [51]. Calculations are carried out on a fully structured
 353 hexahedral mesh consisting of 11,253 cells with $y^+ > 30$ along both walls. Refinement
 354 was introduced around the step resulting in the mesh cells sizes of 0.5mm in the x
 355 and y direction, respectively.

Table 2: Table of simulated cases.

Case	Material	d_p [μm]	ρ_p [kg m^{-3}]	Mass loading	St	Re_p
1	glass	150	2500	20% and 40%	7.9	10.1
2	glass	90	2500	20%	3.8	2.9
3	copper	70	8800	10% and 40%	7.4	4.4

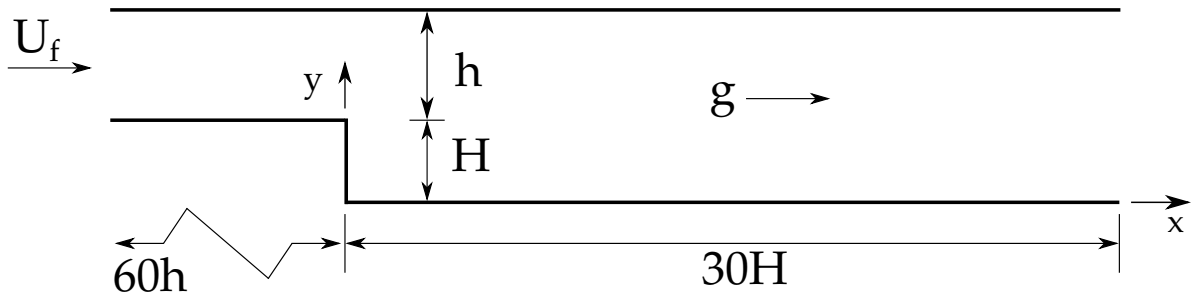


Figure 2: Schematic detailing the geometry used throughout, with $h = 0.02\text{m}$ and $H = 0.0267\text{m}$.

356 **3. Results and Discussion**

357 The simulated results from the RA-TFM and the modified Peirano model (MPM)
 358 are compared against two sets of experimental data given by Fessler and Eaton [19]
 359 & Fessler and Eaton [18]. The MPM equations can be found in the Appendix. Mean
 360 quantities of particle velocity, fluid turbulence intensity and particle turbulence in-
 361 tensity are presented across three cases focusing on three particle classes (see Table
 362 1). The measured velocity profiles start at the recirculation region ($x/H = 2$), con-
 363 tinue through to the reattachment zone ($x/H = 5$), and finally the redevelopment
 364 region ($x/H = 14$) with measurements being taken in between.

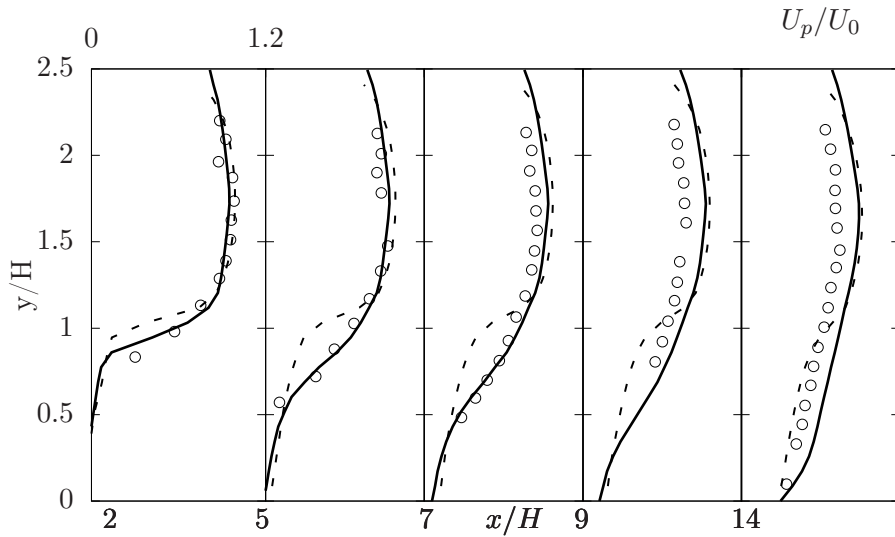


Figure 3: Stream-wise particle mean velocity for case 1. Solid line showing the RA-TFM and the dashed line showing the MPM. Data from Fessler and Eaton [18] with a mass-loading of 40%.

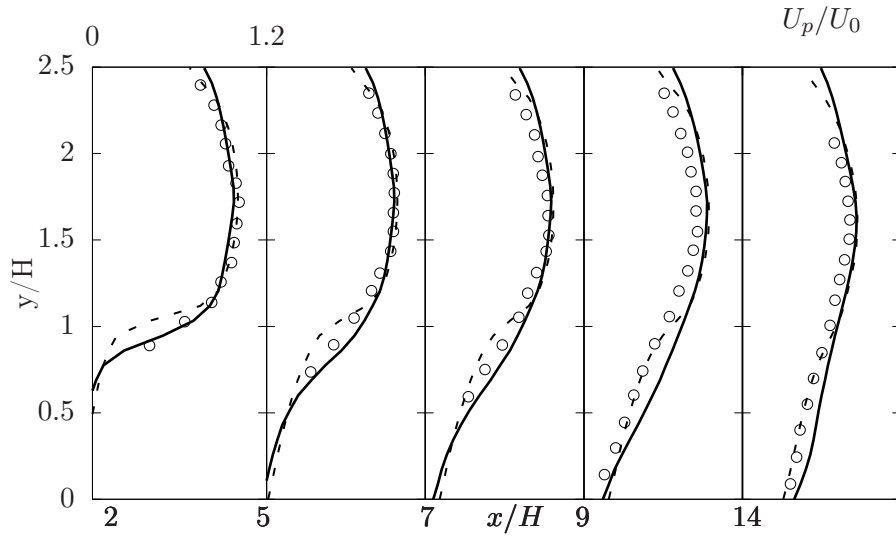


Figure 4: Stream-wise particle mean velocity for case 2. Solid line showing the RA-TFM and the dashed line showing the MPM. Data from Fessler and Eaton [18] with a mass-loading of 20%.

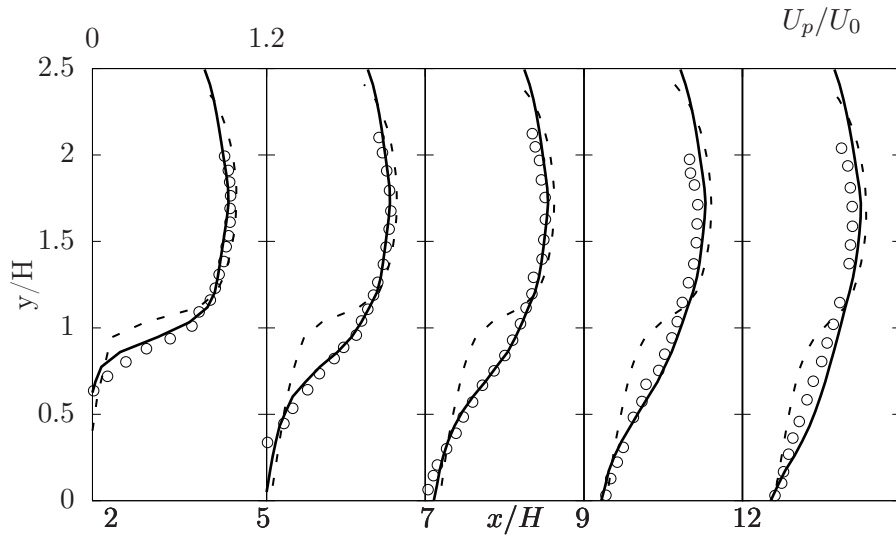


Figure 5: Stream-wise particle mean velocity for case 3. Solid line showing the RA-TFM and the dashed line showing the MPM. Data from Fessler and Eaton [19] with a mass-loading of 10%.

365 *3.1. Mean particle stream-wise velocity*

366 It is evident that across all three Figs. 3, 4 and 5 the prediction of the RA-TFM
 367 mean particle velocity profiles are in good agreement with the measured results. The

368 model captures the affects of varying St and mass loading on the mean velocity pro-
 369 file, especially in the recirculation region corresponding to locations ($x/H = 2$) and
 370 ($x/H = 5$). The MPM shows a marked difference around the step ($0.5 < y/H \leq 1$)
 371 as it does not include the correlated particle turbulent kinetic fluctuations. These
 372 stresses are responsible for forming the shear layer and leading to the production of
 373 turbulent viscosity.

374 All three Figs. 3, 4 and 5 show particle velocities with a flatter gradient across
 375 the depth of the pipe when compared to the fluid velocities, a feature that is not
 376 predicted by the MPM. This is attributed to the calculation of the particle phase
 377 viscosity. In the RA-TFM the calculation of the turbulent viscosity μ_{pt} appearing in
 378 the momentum equation is given by the $k_p - \varepsilon_p$ turbulence model, which accounts
 379 for the correlated turbulent kinetic particle fluctuations that are dominant due to
 380 the shear layer. In the MPM the viscosity is calculated directly from the granular
 381 temperature equation which relies on constitutive closures of thermal conductivity,
 382 shear viscosity and bulk viscosity [40]. As a result, a small value of both is predicted
 383 due to the dilute nature of the flow and this leads to a gross under-prediction of the
 384 particle viscosity. This then allows the momentum coupling term β to dominate in
 385 this region, which is why the mean velocity profiles tend to closely follow the fluid
 386 phase mean velocity profile.

387 Figs. 3 & 5 reveal the largest variation between the predicted mean particle ve-
 388 locity profiles in the shear layer. This is attributed to the particles St , which varies
 389 considerably over the shear layer as shown in both Figs ($y/H < 1$). When the par-
 390 ticles $St \gg 1$ the particles tend to escape from the eddy they are in and ignore the
 391 influence of external eddies. This can either unite small eddies to create larger more
 392 energetic eddies or it can destroy large eddies which dissipate to smaller eddies. As
 393 a consequence of this for $St \gg 1$ we can expect the particle to take longer to react
 394 to the fluid. Therefore, when considering the shear layer the fluid response time, τ_f
 395 will be small in comparison with the channel flow resulting in a much higher local
 396 St . As a result the particle mean velocity profile does not show the sharp gradient
 397 across the ($y/H > 1$) and becomes much flatter.

398 Fig. 3 shows the case denoting both a high St (7.9) and a large mass loading
 399 (40%). It also corresponds to the largest over-prediction in the mean particle ve-
 400 locities at locations ($x/H = 9$ & 14) for the RA-TFM. These locations correspond
 401 to the redevelopment region which indicate that the energy in the particle phase is
 402 recovering too quickly in comparison to the measured data. This overestimation is
 403 difficult to explain as the predictions for case 3 with a large St are in good agree-
 404 ment. One potential source of error could be due to the distribution of the particles
 405 across the width of the pipe. As the particles pass the step they are redistributed

406 inhomogeneously (clustered) which reduces the slip velocity and as a result the drag.
 407 As the particles reach the redevelopment region they begin to redistribute homoge-
 408 neously which increases the drag in this region. However neither model considers the
 409 effects of clustering in their drag model and are only representative of one particle.
 410 This can cause the observed over-estimation of the mean stream-wise velocities in
 411 the redevelopment region.

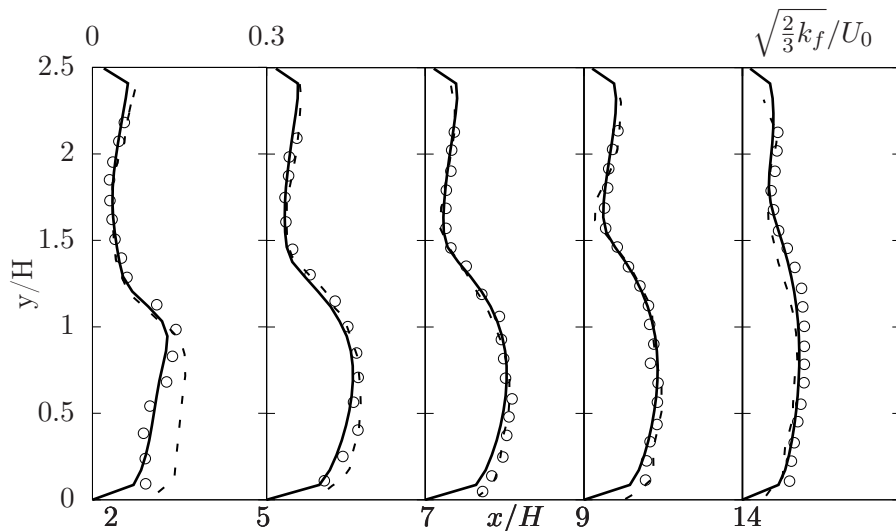


Figure 6: Fluid turbulent intensity for case 1. Solid line showing the RA-TFM and the dashed line showing the MPM. Data from Fessler and Eaton [19] with a mass-loading of 40%.

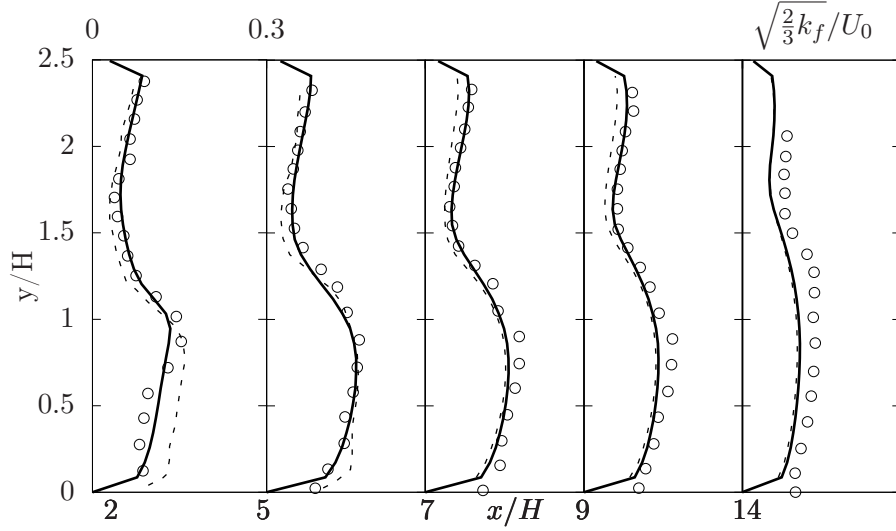


Figure 7: Fluid turbulent intensity for case 2. Solid line showing the RA-TFM and the dashed line showing the MPM. Data from Fessler and Eaton [19] with a mass-loading of 20%.

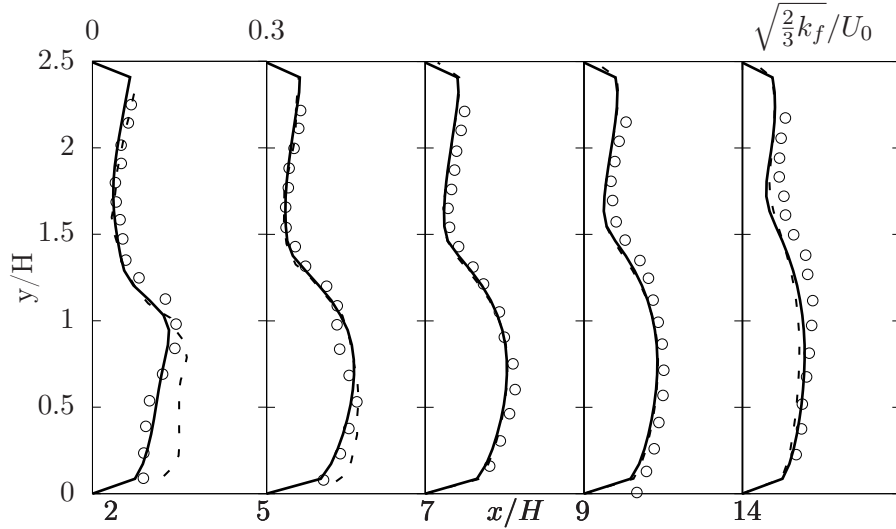


Figure 8: Fluid turbulent intensity for case 3. Solid line showing the RA-TFM and the dashed line showing the MPM. Data from Fessler and Eaton [19] with a mass-loading of 40%.

412 *3.2. Fluid phase turbulence*

413 As shown in the experiment of Fessler and Eaton [19], distinct turbulence atten-
 414 uation was found for the two larger St cases (1 & 3). Over the region of ($y/H > 1$)

415 extensive turbulence attenuation is shown across all five plots (corresponds to Fig.
 416 9 in Fessler and Eaton [19]). Across locations ($x/H = 2$ & 5) there is attenuation
 417 across the range ($y/H > 1$) which shows that as mass loading is increased the tur-
 418 bulence is suppressed and below this range ($y/H < 1$) the turbulence is unaffected.
 419 This behaviour of turbulence attenuation was accurately predicted by the RA-TFM
 420 and the corresponding plots to those in [19] are Figs 6 & 8. The predictions are in
 421 good agreement with the experimental measurements. The turbulence attenuation
 422 for case 1 is as much as 35% showing a large reduction over the region of ($y/H > 1$)
 423 at ($x/H = 2$) on Fig. 8.

424 Below ($y/H < 1$) very little turbulence attenuation was observed, this corresponds
 425 to the shear layer and recirculation zone. From the simulations carried out, the par-
 426 ticle turbulent quantities k_p & ε_p are produced and dissipated primarily near and at
 427 the wall and step (shear layer), with the contribution in the recirculation zone (y/H
 428 < 1) being several orders of magnitudes smaller. When considering the form of the
 429 coupling terms (see Section 2) it is evident why the turbulence attenuation is small
 430 in this region. This also follows from the lack of particles within the recirculation
 431 region due to the large St of all cases ($St > 1$) as the particles are not dragged into
 432 the eddy in the same way a particle of ($St < 1$) would.

433 The turbulence attenuation was accurately captured across all three particle
 434 classes for the RA-TFM. For the MPM an over-prediction of the fluid turbulent
 435 kinetic energy was observed. It was found that the form of the velocity corre-
 436 lation coupling term posed two major problems, the first being that as the term
 437 $k_{fp} = \sqrt{k_f \Theta_p}$ contains Θ_p directly the evolution of the term is adversely affected as
 438 the granular temperature equation evolves too quickly. This behaviour is recognised
 439 in two fluid model codes, and typically an upper limit is employed to constrain the
 440 initial stages of the solution to increase robustness.

441 Secondly, the source term of this form exists in both the k & ε transport equa-
 442 tions, this leads to the formulation of the turbulent kinetic energy dissipation equa-
 443 tion given by Elghobashi and Abou-Arab [16], which has been shown to yield in-
 444 correct behaviour [21], mainly as a consequence of failing to differentiate between
 445 the correlated and uncorrelated turbulent kinetic energy. Conversely, two coupling
 446 source terms are used in this work k_{fp} and ε_{fp} respectively. This allows the coupling
 447 of the turbulent kinetic energy k_i and dissipation ε_i equations of both phases to
 448 contain source terms that are of the same physical attribute i.e. particle turbulent
 449 kinetic energy and particle turbulence kinetic energy dissipation both contain sepa-
 450 rate coupling terms, which ensures conservation of energy between the two phases.
 451 In addition to this no numerical limiting was needed as the evolution of the granular
 452 temperature was controlled by the production of turbulent kinetic energy dissipation.

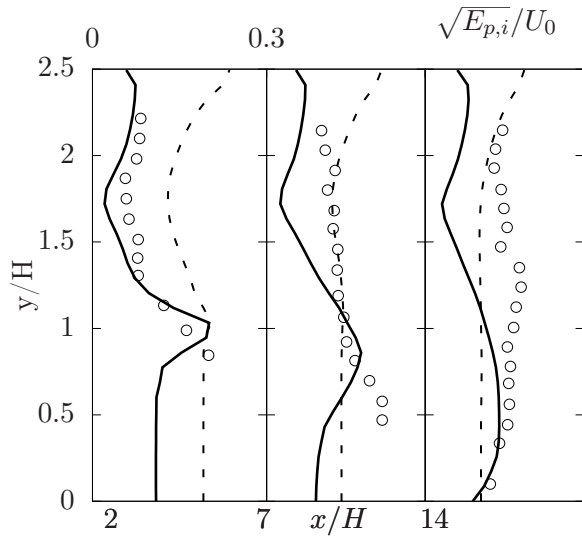


Figure 9: Particle turbulent intensity for case 1. Solid line showing the RA-TFM and the dashed line showing the MPM. Data from Fessler and Eaton [18] with a mass-loading of 40%.

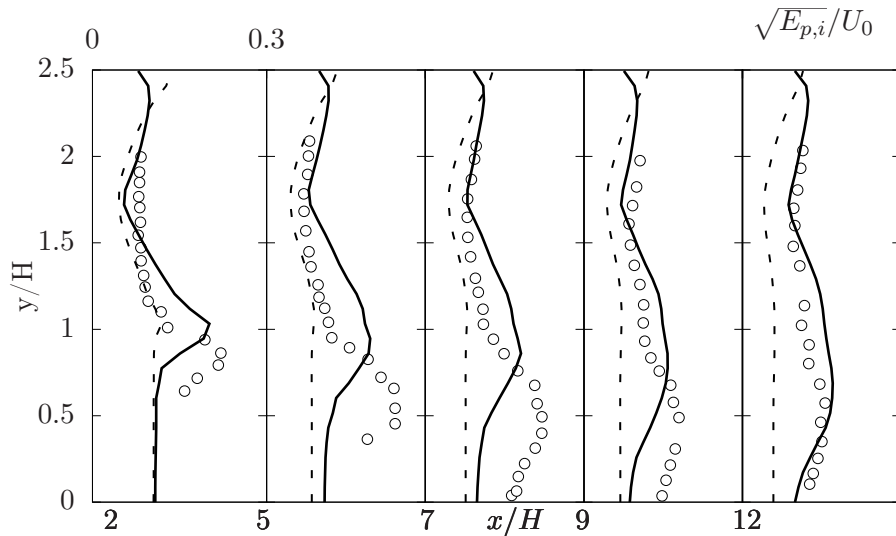


Figure 10: Particle turbulent intensity for case 3. Solid line showing the RA-TFM and the dashed line showing the MPM. Data from Fessler and Eaton [19] with a mass-loading of 10%.

453 *3.3. Particle phase turbulence*

454 From the experimental measurements it can be seen that the particles are being
 455 heavily influenced by the fluid phase's shear layer. This is true for both cases in-
 456 volving large St as shown in Fig 9 & 10. Looking at the results from the MPM the

457 prediction of the shear layer can not be seen across each location. Conversely, the
 458 RA-TFM is able to predict the presence of the shear layer and crucially convect it
 459 downstream. This feature is difficult to predict as the particles disperse and their
 460 fluctuating energy becomes more uniform across the profile. This result was almost
 461 exclusively attributed to the solution of the $k_p - \varepsilon_p$ transport equation.

462 As shown in Février et al. [20] the decomposition of the particle fluctuation en-
 463 ergy into two components which reads, $\kappa_p = k_p + 3/2\Theta_p$ (following the notation
 464 of [21]) was needed when accounting for the particle’s overall motion. Due to the
 465 step, turbulent scales at the integral scale are dominating the flow and as a result
 466 the large scale motions are the most relevant. This is reflected in the predictions
 467 of this model and highlighted when contrasted with the predictions of the MPM.
 468 Without the $k_p - \varepsilon_p$ transport model, the influence of the step is not captured and
 469 an under-prediction of the turbulent particle kinetic energy is seen. Table 3 shows
 470 the integral time scales associated with both flow regimes. This characteristic time
 471 scale associated with the particle turbulent kinetic energy enables the prediction of
 472 the shear layer and allows for the successful prediction of the predominant turbulent
 473 behaviour found in experiment across both Figs. 9 & 10.

Table 3: Table of integral time scales for each phase.

Flow regime	T_p	T_f
Channel flow centre line	0.04s	0.04s
Shear layer	4.09ms	5.12ms

474 In the MPM this definition of the particle-phase time scale is not present. The
 475 calculation of turbulent kinetic energy (granular temperature Θ_p) is heavily reliant on
 476 the constitutive relation of thermal conductivity, shear viscosity and bulk viscosity.
 477 As shown in both Figs. 9 & 10 the absence of the shear layer is demonstrated. The
 478 profiles are within the correct order of magnitude but the profile remains flat and
 479 largely unaffected by the step.

480 The $k_p - \varepsilon_p$ transport equation is modelled in an analogous manner to the single-
 481 phase $k - \varepsilon$ turbulence model using similar closure relations [41]. As a result some
 482 of the models well-known limitations are directly inherited. The Boussinesq approx-
 483 imation is one such limitation of RANS models of this form and introduces isotropy
 484 into the model; specifically the Reynolds stresses are assumed to be a scalar function
 485 of the mean velocity gradients. This introduction of isotropy has quite clear impli-
 486 cations for the prediction of turbulent structures. The shear layer simulated in this
 487 studied is dominated by both the production term, Π_p and the turbulent dissipation

488 term, ε_p ; the former is where the isotropy is introduced and that is why it is so influ-
 489 ential. It has been shown by Simonin [44, 45] that the particle turbulence Reynold
 490 stresses are highly anisotropic and require transport equations for each term. This
 491 is a clear limitation of the current model and from the performance of the current
 492 RA-TFM an introduction of anisotropy for at least the particle phase is vital in an
 493 accurate prediction of the particle phase energy behaviour. Recently, Capecelatro
 494 et al. [7, 8] has derived a multiphase Reynolds-stress model which could fill this gap.
 495 Its application to a flow configuration similar to the one used in this work would be
 496 particularly interesting.

497 *3.4. Particle wall boundary conditions*

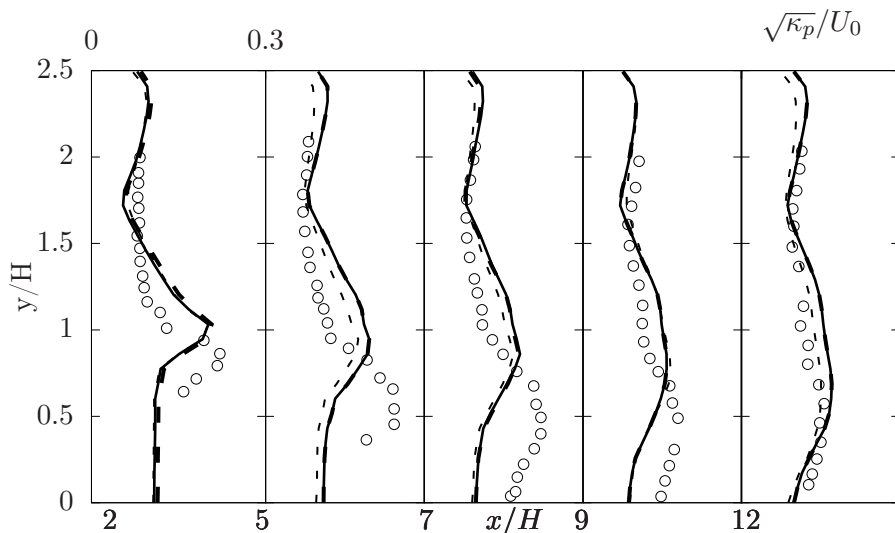


Figure 11: Particle turbulent intensity for case 3. Solid line showing the $\phi = 0.001$, thick dashed line showing $\phi = 0.01$ and the thin dashed line showing $\phi = 0$. Data from Fessler and Eaton [19] with a mass-loading of 10%.

498 As noted in Fessler and Eaton [19], the particles tend to conserve almost all
 499 their energy when interacting with the wall and consequently spend very little time
 500 interacting with it. As a consequence of this observation the specularity coefficient
 501 was varied from 0-0.01 in order to ascertain its effect on the numerical predictions.

502 Fig. 11 shows the particle turbulent intensity prediction of the RA-TFM with
 503 varying specularity coefficients. Immediately a general observation can be made;
 504 the particle phase wall boundary conditions have a relatively small impact on the
 505 prediction of particle fluctuation energy. This is to be expected as the particles

506 spend very little time interacting with the wall and the particle fluctuation energy
507 is dominated by the production in the shear layer.

508 The biggest difference can be seen by comparing $\phi = 0$ with $\phi = 0.01 - 0.001$,
509 and looking at locations ($x/H = 5 - x/H = 12$). The free slip condition exerts its
510 influence on the prediction immediately downstream of the shear layer, this results
511 in an underestimation in comparison with the larger ϕ values. When comparing
512 this result with the experimental data it seems that the prediction lies closer to the
513 measured values, this is seen most clearly at location ($x/H = 5$) across ($y/H > 1$)
514 and across the whole profile at location ($x/H = 12$).

515 When comparing the near wall predictions of particle fluctuation energy it can
516 be seen that there is a slight under-prediction when comparing $\phi = 0$ and $\phi =$
517 $0.01 - 0.001$. This is to be expected as a higher specular coefficient will result in
518 a higher value of particle fluctuation energy due to the production of mean particle
519 shear. All three simulations under-predict the near wall behaviour, this result is
520 attributed to the lack of particle phase fluctuation anisotropy, but put more explicitly
521 the experimental observations show that the particle fluctuation energy is stretched
522 in the wall-normal direction. This stretching continues up to the wall (at $x/H =$
523 7), the RA-TFM used in this work can not predict this behaviour due to the inherit
524 assumptions made throughout.

525 A specular coefficient value of 0.1 was tested but yielded unphysical results.
526 [3, 61] also found that a low specular coefficient was representative of high velocity,
527 dilute fluid-particle flow. The unphysical results were due to the lowering of the slip
528 velocity near the wall. The mean velocity profiles for the fluid and particle phase
529 tend to converge as the no slip condition ($\phi = 1$) is approached. At the relatively
530 high speed velocities used in this study this resulted in a gross overestimation of
531 the particle fluctuation energy. An explanation for this behavior is as follows, the
532 high specular coefficient at the wall promotes "sticking" of the particles. As these
533 particles are stuck at the wall and then released they begin to produce mean shear
534 in the particle phase momentum equation. This shearing which is imposed by the
535 boundary condition results in an overestimation of turbulence production resulting
536 in excessively large values of the particle phase fluctuation energy.

537 *3.5. RA-TFM discussion*

538 Given the plethora of terms required to close the RA-TFM, a discussion of the
539 relevant and negligible terms is warranted. The discussion is confined to the closure
540 modelled terms with transport, convective and Laplacian terms omitted. We begin
541 our discussion by focusing on the turbulent dispersion/drag/drift term which can
542 be found in Eq. 2 & 4 of Section 2. Throughout the study this term remained

543 negligible and this was true for both the glass particles of case 1 & 2 and the copper
544 particles of case 3. The reasons for this are two-fold: across the width of the pipe
545 the gradient of the volume fraction remains small due to the uniformity imposed
546 by gravity. This uniformity of the particle volume fraction across the pipe width of
547 near identical conditions has also been reported by Vreman [54] & Yamamoto et al.
548 [57]. This uniformity changes in the presence of the shear layer as there is a smaller
549 particle volume fraction in the recirculating region than in the shear layer. This
550 large particle volume fraction gradient is directly opposed by the increase of the St,
551 as highlighted previously in Section 3.1 the St increases dramatically in the shear
552 layer thus decreasing the amount of dispersion.

553 Next, the turbulent pressure term, which contains the term $2/3\rho_p\alpha_pk_p$, remains
554 negligible throughout. This term arises due to compressibility effects which are
555 expected to be high for large Mach numbers, which was not the case in this work.
556 The covariance of the volume fraction and fluid pressure gradient remains very small
557 throughout; this was to be expected as it represents the fluctuations in the buoyancy
558 force. Due to the high density ratio, ρ_p/ρ_f the flow was not considered buoyancy
559 driven and so this term was negligible.

560 The velocity-fluid-pressure-gradient covariance term was found to be negligible for
561 glass particles but was vital in the successful prediction of the mean particle velocities
562 of the copper particles. In fact, without this term the mean particle velocities were
563 over-predicted by up to 10%. If we revisit this term it becomes clear as to why;
564 the term takes the form $\alpha_p\rho_p\mathbf{g}$ (neglecting the constant density ratio) and when the
565 particle volume fraction is present there is a static pressure gradient of the particles
566 acting on the mean momentum of both the particle and fluid phase. This means that
567 the mean slip velocity is affected by the imposed pressure gradient. In this work it
568 resulted in a reduction of the mean particle velocities. Consequently, this term can
569 not be neglected for particles with large densities or (put more generally) for large
570 St.

571 For the multiphase turbulence modelling coupling terms found in Eq. 5, 6, 10 &
572 11, only the velocity correlation terms were found to be relevant for this flow. These
573 terms are responsible for the turbulence attenuation, so it follows that they should
574 remain. The volume-fraction-velocity correlation was found to be negligible due to
575 the high density ratio used in this work, but for small density ratios this term may be
576 relevant. The mean slip term was found to be non-negligible but its magnitude was
577 not enough to affect the solution. Interestingly, in this work there was a large mean
578 slip value near the wall which is where this term is expected to be at its largest. Due
579 to the use of single-phase wall functions this behaviour may have been suppressed
580 resulting in an underestimation.

581 Finally, a note on the limitations of the current approach. As shown in Fox [21] the
582 hydrodynamic model (volume fraction, particle velocity and granular temperature)
583 is derived from the mesoscale model i.e the Boltzmann equation, using a Chapman-
584 Enskog expansion (shown in Garzó et al. [22]) in powers of Knudsen number. It
585 is owing to this mathematical linearisation that the hydrodynamical model is not
586 valid for large values of Knudsen number ($\text{Kn} > 1$). The hydrodynamical model, as
587 hinted at, is therefore most accurate for small values of Knudsen number ($\text{Kn} \ll 1$),
588 a feature of collisionally dominated flows (see Table 4 for Kn).

589 The flow regime used in this study is characterized as moderately dilute where
590 collisions are expected. For the smallest mass loading (case 3), the Knudsen number
591 was found to be ($\text{Kn} < 10^{-4}$) across the pipe, whilst for higher mass loadings the
592 Knudsen number was much lower. As this constraint is one across the whole domain
593 this can not always be fulfilled. When considering a fluidised bed for example, the
594 upper region of the chamber will not fulfill this criteria as no collisions are present as
595 there are no particles. For this study the recirculating region posed a problem as only
596 a small number of particles were present in the region. This meant that in this region
597 the Knudsen number would fluctuate due to the vortex shedding and temporarily
598 be $\mathcal{O}(1)$, compromising the validity of the solution. It was found that the value of
599 granular temperature was relatively high which may have allowed for near equilibrium
600 conditions thus satisfying the hydrodynamic constraint. Unfortunately, this type of
601 constraint is unavoidable when employing a hydrodynamical description and this can
602 not necessarily be fulfilled in every region of the flow. For a more flexible approach,
603 kinetic-based equations can be formulated from moments (see [5, 32, 35, 39]).

604 4. Conclusions

605 The current work has investigated turbulent attenuation of moderately dilute flow
606 in a vertically orientated backward-facing step using a Reynolds-Averaged Two-Fluid
607 model. The RA-TFM model is implemented into OpenFOAM with the implementa-
608 tion procedure and the treatment of challenging terms provided. The model results
609 are compared against benchmark experimental data and also against the model of
610 Peirano and Leckner [40]. A summary of our findings are as follows:

- 611 1. Prediction of the mean particle velocities and both turbulence quantities (tur-
612 bulent kinetic energy of the fluid and particles) were in good agreement with
613 the benchmark experimental data.
- 614 2. The inclusion of the correlated k_p and uncorrelated Θ_p particle motion was
615 crucial in accurately predicting the behaviour of the turbulent shear layer.
616 This was further highlighted when compared to the turbulent particle kinetic
617 energy predictions from the modified Peirano model.
- 618 3. The form of the velocity correlation coupling terms, i.e. separate coupling
619 terms for turbulent kinetic energy and turbulent kinetic energy dissipation,
620 resulted in a successful prediction of turbulence attenuation.
- 621 4. A specularly coefficient value of 0.001 was found to be representative of the
622 particle-wall behaviour in this study. Changes in the specularly coefficient (ϕ
623 < 0.01) had very little effect on the particle fluctuation energy prediction.
- 624 5. It has been shown that the behaviour of the particles interacting in a shear layer
625 is highly anisotropic. The current predictions of this behaviour are limited due
626 to the reliance on the Boussinesq approximation which introduces isotropy into
627 the model.

628 **Nomenclature**

U_0	centreline velocity, [ms^{-1}]
C_D	drag coefficient, [-]
A_i	diagonal coefficients of the matrix
g	gravity, [ms^{-2}]
\mathbf{n}	unit vector normal to the wall, [-]
Re_p	particle Reynolds number, [-]
d_p	particle diameter, [m]
\mathbf{u}_i	velocity, [ms^{-1}]
\mathbf{u}_w	wall velocity, [ms^{-1}]
$\mathbf{u}_{p,w}$	particle slip velocity parallel to the wall, [ms^{-1}]
\mathbf{u}_p''	particle velocity fluctuation w.r.t PA velocity, [ms^{-1}]
$\mathbf{u}_{p,i}''^2$	particle Reynolds stress component in direction i, [ms^{-1}]
\mathbf{u}_f'''	fluid velocity fluctuation w.r.t PA velocity, [ms^{-1}]
h	pipe width, [m]
p_i	pressure, [Pa]
g_0	radial distribution coefficient, [-]
H	step height, [m]
t	time, [s]
k_i	turbulent kinetic energy, [m^2s^{-2}]

629 *Greek letters*

α_i	volume fraction, $[-]$
$\alpha_{p,max}$	maximum particle volume fraction, $[-]$
β	momentum exchange coefficient, $[\text{kgm}^{-3}\text{s}^{-1}]$
ε_i	turbulent kinetic energy dissipation, $[\text{m}^2\text{s}^{-3}]$
Θ_p	granular temperature, $[\text{m}^2\text{s}^{-2}]$
κ_p	particle fluctuation energy, $[\text{m}^2\text{s}^{-2}]$
κ_{Θ_s}	diffusion coefficient for granular energy, $[\text{kgm}^{-1}\text{s}^{-1}]$
μ_i	shear viscosity, $[\text{kgm}^{-1}\text{s}^{-1}]$
$\mu_{i,t}$	turbulent shear viscosity, $[\text{kgm}^{-1}\text{s}^{-1}]$
ν_i	kinematic viscosity, $[\text{m}^2\text{s}^{-1}]$
$\nu_{i,t}$	turbulent kinematic viscosity, $[\text{m}^2\text{s}^{-1}]$
ρ_i	density, $[\text{kgm}^{-3}]$
$\overline{\sigma}_f$	fluid phase stress tensor, $[\text{kgm}^{-1}\text{s}^{-2}]$
$\overline{\sigma}_p$	particle phase stress tensor, $[\text{kgm}^{-1}\text{s}^{-2}]$
τ_d	particle relaxation time, $[\text{s}]$

630 *Subscripts*

1	RA-TFM
2	MPM
f	fluid
i	general index
p	particle
x	x direction
y	y direction
z	z direction

631 *Superscripts*

"	PA particle velocity fluctuation
'''	PA fluid velocity fluctuation

632 *Special notation*

$\langle \cdot \rangle$	Reynolds averaging operator
$\langle \cdot \rangle_i$	phase averaging operator associated with phase i

Table 4: Model characteristics.

$$\beta = \frac{\rho_p \alpha_p}{\tau_d} = \frac{3}{4} \frac{\alpha_p \alpha_f \rho_f \mathbf{u}_r}{d_p} C_d$$

$$C_d = \begin{cases} \frac{24}{Re_p} [1 + 0.15 Re_p^{0.287}] & \text{if } Re_p < 1000 \\ 0.44 & \text{if } Re_p \geq 1000 \end{cases}$$

$$Re_p = \frac{\rho_f d_p |\mathbf{u}_p - \mathbf{u}_f|}{\mu_f}$$

$$E_{p,1} \equiv \kappa_p = k_p + 3/2 \Theta_p$$

$$E_{p,2} \equiv \kappa_p = 3/2 \Theta_p$$

$$\tau_f \equiv T_f = k_f / \varepsilon_f$$

$$St = \tau_d / \tau_f$$

$$T_p = \frac{k_p}{\varepsilon_p}$$

$$Kn = \frac{\sqrt{\pi} d_p}{12 \alpha_p g_0 L}$$

$$\chi = \frac{\alpha_p \rho_p}{\alpha_f \rho_f}$$

$$e = 0.9$$

Table 5: Definition of variables.

$$\kappa_p = k_p + 1.5\Theta_p$$

$$\mu_f = \rho_f \nu_f$$

$$\mu_{ft} = \alpha_f \rho_f \nu_{ft} = \alpha_f \rho_f C_{f\mu} \frac{k_f^2}{\varepsilon_f}$$

$$\mu_p = \alpha_p \rho_p \nu_p = \frac{2\mu_{pdil}}{(1+e)g_0} \left[1 + \frac{4}{5}(1+e)g_0\alpha_p \right]^2 + \frac{4}{5}\alpha_p^2 \rho_p d_p g_0 (1+e) \left(\frac{\Theta_p}{\pi} \right)^{1/2}$$

$$\mu_{pdil} = \frac{5\sqrt{\pi}}{96} \rho_p d_p \Theta_p^{1/2}$$

$$\mu_{pt} = \alpha_p \rho_p \nu_{pt} = \alpha_p \rho_p C_{p\mu} \frac{k_p^2}{\varepsilon_p}$$

$$p_p = \rho_p \alpha_p \Theta_p + 2(1+e)\rho_p \alpha_p^2 g_0 \Theta_p$$

$$\gamma = \frac{12(1-e^2)g_0}{\sqrt{\pi}d_p} \alpha_p^2 \rho_p \Theta_p^{3/2}$$

$$\kappa_\Theta = \frac{2}{(1+e)g_0} \left[1 + \frac{6}{5}(1+e)g_0\alpha_p \right]^2 \kappa_{\Theta,dil} + 2\alpha_p^2 \rho_p d_p g_0 (1+e) \left(\frac{\Theta_p}{\pi} \right)^{1/2}$$

$$\kappa_{\Theta,dil} = \frac{75}{384} \sqrt{\pi} \rho_p d_p \Theta_p^{1/2}$$

$$g_0 = \left[1 - \left(\frac{\alpha_p}{\alpha_{p,max}} \right)^{\frac{1}{3}} \right]^{-1}$$

$$\bar{\mathbf{S}}_p = \frac{1}{2} [\nabla \mathbf{u}_p + (\nabla \mathbf{u}_p)^T] - \frac{1}{3} \nabla \cdot \mathbf{u}_p \mathbf{I}$$

$$\bar{\mathbf{S}}_f = \frac{1}{2} [\nabla \mathbf{u}_f + (\nabla \mathbf{u}_f)^T] - \frac{1}{3} \nabla \cdot \mathbf{u}_f \mathbf{I}$$

$$k_{fp} = \beta_k \sqrt{k_f k_p}$$

$$\varepsilon_{fp} = \beta_\varepsilon \sqrt{\varepsilon_f \varepsilon_p}$$

Table 6: Definition of phase-averaged variables.

$$\alpha_p = \langle \alpha_p \rangle$$

$$\alpha_f = \langle \alpha_f \rangle$$

$$\mathbf{u}_p = \langle \mathbf{u} \rangle_p$$

$$\mathbf{u}_f = \langle \mathbf{u} \rangle_f$$

$$\Theta_p = \langle \Theta \rangle_p$$

$$k_p = \frac{1}{2} \langle \mathbf{u}_p'' \cdot \mathbf{u}_p'' \rangle_p$$

$$k_f = \frac{1}{2} \langle \mathbf{u}_f''' \cdot \mathbf{u}_f''' \rangle_f$$

$$\varepsilon_p = \frac{1}{\rho_p \alpha_p} \langle \bar{\boldsymbol{\sigma}}_p : \nabla \mathbf{u}_p'' \rangle$$

$$\varepsilon_f = \frac{1}{\rho_f \alpha_f} \langle \bar{\boldsymbol{\sigma}}_f : \nabla \mathbf{u}_f''' \rangle$$

$$\bar{\boldsymbol{\sigma}}_p = \mu_p [\nabla \mathbf{u}_p + (\nabla \mathbf{u}_p)^T] - \frac{1}{3} \mu_p \nabla \cdot \mathbf{u}_p \mathbf{I}$$

$$\bar{\boldsymbol{\sigma}}_f = \mu_f [\nabla \mathbf{u}_f + (\nabla \mathbf{u}_f)^T] - \frac{1}{3} \mu_f \nabla \cdot \mathbf{u}_f \mathbf{I}$$

$$\mathbf{u}_p'' = \mathbf{u}_p - \langle \mathbf{u}_p \rangle_p$$

$$\mathbf{q}_\Theta = \langle \mathbf{q}_\Theta \rangle_p = \frac{\kappa_\Theta}{\alpha_p \rho_p} \nabla \Theta_p$$

$$\mathbf{u}_f''' = \mathbf{u}_f - \langle \mathbf{u}_f \rangle_f$$

$$\langle \mathbf{u}_p \rangle_p = \langle \alpha_p \mathbf{u}_p \rangle / \langle \alpha_p \rangle$$

$$\langle \mathbf{u}_f \rangle_f = \langle \alpha_f \mathbf{u}_f \rangle / \langle \alpha_f \rangle$$

$$\mathbf{u}_p'' \mathbf{u}_p'' = \langle \mathbf{u}_p'' \mathbf{u}_p'' \rangle_p$$

633 **5. Appendix**

634 Here the equations used in the MPM are presented. A full explanation of the
 635 equations can be found in Peirano and Leckner [40]. The modification of the model
 636 comes from the type of closure for the particle-fluid covariance in which the isotropic
 637 model of Sinclair and Mallo [46] is used.

638 The continuity equations for each phase read:

639
$$\frac{\partial \alpha_p \rho_p}{\partial t} + \nabla \cdot \alpha_p \rho_p \mathbf{u}_p = 0 \quad (42)$$

640
 641
$$\frac{\partial \alpha_f \rho_f}{\partial t} + \nabla \cdot \alpha_f \rho_f \mathbf{u}_f = 0 \quad (43)$$

642
 643 The momentum balance equation for each phase:

644
$$\frac{\partial \alpha_p \rho_p \mathbf{u}_p}{\partial t} + \nabla \cdot \alpha_p \rho_p \mathbf{u}_p \mathbf{u}_p = \alpha_p \nabla \cdot \tau_p - \alpha_p \nabla p_f - \nabla p_p + \beta(\mathbf{u}_f - \mathbf{u}_p) + \alpha_p \rho_p \mathbf{g} \quad (44)$$

645
 646
$$\frac{\partial \alpha_f \rho_f \mathbf{u}_f}{\partial t} + \nabla \cdot \alpha_f \rho_f \mathbf{u}_f \mathbf{u}_f = \alpha_f \nabla \cdot \tau_f - \alpha_f \nabla p_f - \beta(\mathbf{u}_p - \mathbf{u}_f) + \alpha_f \rho_f \mathbf{g} \quad (45)$$

647 *5.1. Kinetic Theory of Granular Flow*

648 Following the kinetic theory of granular flow the closure of the particle pres-
 649 sure, shear and bulk viscosities can be provided. The granular temperature Θ_p
 650 is introduced as a measure of the particle velocity fluctuations [23].

$$\Theta_p = \frac{1}{3} \mathbf{u}_p''^2 \quad (46)$$

651 where \mathbf{u}_p'' is the particle fluctuation velocity. A balance equation is introduced for
 652 the granular energy ($\frac{3}{2}\Theta_p$) to satisfy the continuity and momentum balance for both
 653 phases. The fluctuation energy conservation for the particles is then given as:

$$\frac{3}{2} \left[\frac{\partial \alpha_p \rho_p \Theta_p}{\partial t} + \nabla \cdot \alpha_p \rho_p \Theta_p \mathbf{u}_p \right] = (p_p \bar{\bar{I}} + \bar{\bar{\tau}}) : \nabla \mathbf{u}_p + \nabla \cdot \kappa \nabla \Theta_p - \gamma_p + J_{vis} + J_{slip} \quad (47)$$

654 where the first term on the RHS is the fluctuation energy created by the shearing in
 655 the particle phase. The second term is associated with the diffusion of fluctuating
 656 energy, the third term is responsible for the dissipation due to inelastic collisions.

657 Finally, J_s is either dissipation of granular temperature due to viscous damping
 658 and/or creation of granular temperature from the slip between the fluid and particles.
 659 Both terms can be written more intuitively to read:

$$J_{vis} + J_{slip} = \beta(\mathbf{u}_p''\mathbf{u}_p'' - \mathbf{u}_p''\mathbf{u}_f''') \quad (48)$$

660 The first term can be modeled as $3\Theta_p$ according to Gidaspow [23] and the last term
 661 can be modeled as k_{pf} .

662 5.2. Turbulence modelling

663 The transport equations for the fluid phases turbulence model $k_f - \varepsilon_f$ reads as
 664 follows:

$$\frac{\partial \alpha_f \rho_f k_f}{\partial t} + \nabla \cdot \alpha_f \rho_f k_f \mathbf{u}_f = \nabla \cdot \alpha_f \rho_f \nu_t \nabla k_f + \alpha_f G - \alpha_f \rho_f \varepsilon_f + \Pi_{kf} \quad (49)$$

665

$$\frac{\partial \alpha_f \rho_f \varepsilon_f}{\partial t} + \nabla \cdot \alpha_f \rho_f \varepsilon_f \mathbf{u}_f = \nabla \cdot \alpha_f \rho_f \nu_t \nabla \varepsilon_f + \frac{\varepsilon_f}{k_f} \left[C_1 \alpha_f G - C_2 \alpha_f \rho_f \varepsilon_f + C_3 \Pi_{kf} \right] \quad (50)$$

666 Where G is the production of the turbulent kinetic energy, which is expressed as
 667 follows:

$$G = 2\nu\rho_f \left(\overline{\mathbf{S}_f} : \overline{\mathbf{S}_f} - \frac{2}{3} \text{tr}(\overline{\mathbf{S}_f})^2 \cdot \mathbf{I} \right) + \frac{2}{3} \rho_f k_f \nabla \cdot (\mathbf{u}_f \mathbf{I}) \quad (51)$$

668 The term Π_{kf} accounts for turbulence modulation from particles and represents the
 669 velocity fluctuation correlation of each phase,

$$\Pi_{kf} = -\beta(2k_f - k_{pf} - \mathbf{u}_r \mathbf{u}_d) \quad (52)$$

670 The term \mathbf{u}_d accounts for turbulence dispersion and is also known as the drift velocity.
 671 Here it is given from the formulation of [44].

$$\mathbf{u}_d = -D_{sf} \left(\frac{1}{\alpha_p} \nabla \alpha_p - \frac{1}{\alpha_f} \nabla \alpha_f \right) \quad (53)$$

672 The fluid-particle covariance term is given by Sinclair and Mallo [46] and is also
 673 termed an isotropic model.

$$k_{pf} = c_{pf} \sqrt{k_f \Theta_p} \quad (54)$$

674 **6. Bibliography**

- 675 [1] Anderson, T. B. and Jackson, R. (1967). Fluid mechanical description of fluidized
676 beds: Equations of Motion. *Industrial and Engineering Chemistry Fundamentals*,
677 6(4):527–539.
- 678 [2] Benavides, A. and van Wachem, B. (2008). Numerical simulation and valida-
679 tion of dilute turbulent gas-particle flow with inelastic collisions and turbulence
680 modulation. *Powder Technology*, 182:294–306.
- 681 [3] Benyahia, S., Syamlal, M., and O’Brien, T. J. (2005). Evaluation of boundary
682 conditions used to model dilute, turbulent gas/solids flows in a pipe. *Powder*
683 *Technology*, 156(2):62 – 72. Particle Technology Forum Special Issue.
- 684 [4] Borée, J. and Caraman, N. (2005). Dilute bidispersed tube flow: Role of interclass
685 collisions at increased loadings. *Physics of Fluids*, 17(5):055108.
- 686 [5] Buffo, A., Vanni, M., and Marchisio, D. L. (2016). On the implementation of
687 moment transport equations in OpenFOAM : Boundedness and realizability. *In-*
688 *ternational Journal of Multiphase Flow*, 85:223 – 235.
- 689 [6] Capecelatro, J., Desjardins, O., and Fox, R. O. (2015). On fluid-particle dy-
690 namics in fully developed cluster-induced turbulence. *Journal of Fluid Mechanics*,
691 780:578–635.
- 692 [7] Capecelatro, J., Desjardins, O., and Fox, R. O. (2016a). Strongly coupled
693 fluid-particle flows in vertical channels. I. Reynolds-averaged two-phase turbulence
694 statistics. *Physics of Fluids*, 28(3).
- 695 [8] Capecelatro, J., Desjardins, O., and Fox, R. O. (2016b). Strongly coupled fluid-
696 particle flows in vertical channels. II. Turbulence modeling. *Physics of Fluids*,
697 28(3).
- 698 [9] Caraman, N., Borée, J., and Simonin, O. (2003). Effect of collisions on the
699 dispersed phase fluctuation in a dilute tube flow: Experimental and theoretical
700 analysis. *Physics of Fluids*, 15(12):3602–3612.
- 701 [10] Chan, C. K., Zhang, H. Q., and Lau, K. S. (2001). Numerical simulation of
702 gas-particle flows behind a backward-facing step using an improved stochastic
703 separated flow model. *Computational Mechanics*, 27(5):412–417.

- 704 [11] Dasgupta, S., Jackson, R., and Sundaresan, S. (1994). Turbulent gas-particle
705 flow in vertical risers. *AIChE Journal*, 40(2):215–228.
- 706 [12] Dasgupta, S., Jackson, R., and Sundaresan, S. (1998). Gas-particle flow in
707 vertical pipes with high mass loading of particles. *Powder Technology*, 96(1):6 –
708 23.
- 709 [13] Drew, D. A. and Lahey, R. T. (1993). *In particulate Two-phase Flow*.
710 Butterworth-Heinemann, Boston.
- 711 [14] Elghobashi, S. (1994). On predicting particle-laden turbulent flows. *Applied*
712 *Scientific Research*, 52(4):309–329.
- 713 [15] Elghobashi, S. and Truesdell, G. C. (2006). Direct simulation of particle disper-
714 sion in a decaying isotropic turbulence. *Journal of Fluid Mechanics*, 242(-1):655.
- 715 [16] Elghobashi, S. E. and Abou-Arab, T. W. (1983). A two-equation turbulence
716 model for two-phase flows. *Physics of Fluids*, 26(4):931.
- 717 [17] Ferziger, J. H. and Perić, M. (2002). *Computational Methods for Fluid Dynam-*
718 *ics*. Springer.
- 719 [18] Fessler, J. R. and Eaton, J. K. (1995). Particle-turbulence interaction in a
720 backward-facing step flow. *Rep. MD-70*, 394(1995):97–117.
- 721 [19] Fessler, J. R. and Eaton, J. K. (1999). Turbulence modification by particles in
722 a backward-facing step flow. *Journal of Fluid Mechanics*, 394(1999):97–117.
- 723 [20] Février, P., Simonin, O., and Squires, K. D. (2005). Partitioning of particle
724 velocities in gas solid turbulent flows into a continuous field and a spatially uncor-
725 related random distribution: theoretical formalism and numerical study. *Journal*
726 *of Fluid Mechanics*, 533:1–46.
- 727 [21] Fox, R. O. (2014). On multiphase turbulence models for collisional fluid-particle
728 flows. *Journal of Fluid Mechanics*, 742:368–424.
- 729 [22] Garzó, V., Tenneti, S., Subramaniam, S., and Hrenya, C. M. (2012). Enskog ki-
730 netic theory for monodisperse gas-solid flows. *Journal of Fluid Mechanics*, 712:129–
731 168.
- 732 [23] Gidaspow, D. (1994). *Multiphase flow and fluidization*. Academic Press.

- 733 [24] Gore, R. and Crowe, C. (1989). Effect of particle size on modulating turbulent
734 intensity. *International Journal of Multiphase Flow*, 15(2):279 – 285.
- 735 [25] Helland, E., Occelli, R., and Tadriss, L. (2002). Computational study of fluctu-
736 ating motions and cluster structures in gas-particle flows. *International Journal*
737 *of Multiphase Flow*, 28(2):199 – 223.
- 738 [26] Hetsroni, G. (1989). Particles-turbulence interaction. *International Journal of*
739 *Multiphase Flow*, 15(5):735 – 746.
- 740 [27] Hrenya, C. and Sinclair, J. (1997). Effects of particle-phase turbulence in gas-
741 solid flows. *AIChE Journal*, 43(4):853–869.
- 742 [28] Ishii, M. (1975). Thermo-fluid dynamic theory of two-phase flow. *NASA*
743 *STI/Recon Technical Report A*, 75.
- 744 [29] Issa, R. I. (1986). Solution of the implicitly discretised fluid flow equations by
745 operator-splitting. *Journal of Computational Physics*, 62(1):40–65.
- 746 [30] Jasak, H. (1996). Error Analysis and Estimation for the Finite Volume Method
747 with Applications to Fluid Flows. *PhD Thesis*, Imperial College London(June).
- 748 [31] Johnson, P. C. and Jackson, R. (1987). Friction-collisional constitutive rela-
749 tions for granular materials, with application to plane shearing. *Journal of Fluid*
750 *Mechanics*.
- 751 [32] Kong, B. and Fox, R. O. (2017). A solution algorithm for fluid-particle flows
752 across all flow regimes. *Journal of Computational Physics*, 344:575 – 594.
- 753 [33] Kulick, J., Fessler, J. R., and Eaton, J. R. (1994). Particle response and tur-
754 bulence modification in fully developed channel flow. *Journal of Fluid Mechanics*,
755 277:109–134.
- 756 [34] Liu, X. and Xu, X. (2009). Modelling of dense gas-particle flow in a circulating
757 fluidized bed by distinct cluster method (dcm). *Powder Technology*, 195(3):235 –
758 244.
- 759 [35] Marchisio, D. L. and Fox, R. O. (2013). *Computational Models for Polydisperse*
760 *Particulate and Multiphase Systems*. Cambridge Series in Chemical Engineering.
761 Cambridge University Press.

- 762 [36] Mohanarangam, K. and Tu, J. Y. (2007). Two-fluid model for particle-
763 turbulence interaction in a backward-facing step. *AICHE Journal*, 53(9):2254–
764 2264.
- 765 [37] Moukalled, F., Mangani, L., and Darwish, M. (2015). *The Finite Volume Method*
766 *in Computational Fluid Dynamics: An Advanced Introduction with OpenFOAM*
767 *and Matlab*. Springer Publishing Company, Incorporated, 1st edition.
- 768 [38] Mukin, R. V. and Zaichik, L. I. (2012). Nonlinear algebraic Reynolds stress
769 model for two-phase turbulent flows laden with small heavy particles. *International*
770 *Journal of Heat and Fluid Flow*, 33(1):81–91.
- 771 [39] Passalacqua, A., Fox, R., Garg, R., and Subramaniam, S. (2010). A fully coupled
772 quadrature-based moment method for dilute to moderately dilute fluid-particle
773 flows. *Chemical Engineering Science*, 65(7):2267 – 2283. International Symposium
774 on Mathematics in Chemical Kinetics and Engineering.
- 775 [40] Peirano, E. and Leckner, B. (1998). Fundamentals of turbulent gas-solid flows
776 applied to circulating fluidized bed combustion. *Doktorsavhandlingar vid Chalmers*
777 *Tekniska Hogskola*, 24(1381):259–296.
- 778 [41] Pope, S. B. (2011). *Turbulent flows*. Cambridge Univ. Press, Cambridge.
- 779 [42] Rhie, C. M. and Chow, W. L. (1983). A numerical study of the turbulent flow
780 past an isolated airfoil with trailing edge separation. *AIAA J.*, pages 1525–1532.
- 781 [43] Rusche, H. (2002). Computational Fluid Dynamics of Dispersed Two-Phase
782 Flows at High Phase Fractions. *PhD Thesis*, (December).
- 783 [44] Simonin, O. (1991). Second-moment prediction of dispersed phase turbulence
784 in particle-laden flows. *Proceedings of 8th International Symposium on Turbulent*
785 *Shear Flows*, 1(4):741–746.
- 786 [45] Simonin, O. (1996). Continuum modeling of dispersed turbulent two-phase
787 flows. Part 1: General model description. *Combustion and Turbulence in Two-*
788 *phase Flows*.
- 789 [46] Sinclair, J. and Mallo, T. (1998). Describing particle-turbulence interaction
790 in a two-fluid modeling framework. *Proceedings of FEDSM'98: ASME Fluids*
791 *Engineering Division Summer Meeting*, 4:7–14.

- 792 [47] Soo, S. L. (1990). *Multiphase Fluid Dynamics*. Science Press, Gower Technical,
793 New York.
- 794 [48] Syamlal, M. and O'Brien, T. J. (1989). Computer simulation of bubbles in a
795 fluidized bed. *AIChE Symposium Series*, 85(270):22–31.
- 796 [49] Tanaka, T., Yonemura, S., Kiribayashi, K., and Tsuji, Y. (1996). Cluster for-
797 mation and particle-induced instability in gas-solid flows predicted by the dsmc
798 method. *JSME International Journal Series B*, 39(2):239–245.
- 799 [50] Tsuji, Y. and Morikawa, Y. (1984). LDV measurements of an air-solid two-phase
800 flow in a vertical pipe. *Journal of Fluid Mechanics*, 120:385–409.
- 801 [51] Van Wachem, B. G. M., Schouten, J. C., Van den Bleek, C. M., Krishna, R.,
802 and Sinclair, J. L. (2001). Comparative analysis of CFD models of dense gas-solid
803 systems. *AIChE Journal*, (5).
- 804 [52] Viollet, P. L. and Simonin, O. (1994). Modelling dispersed two-phase flows:
805 Closure, validation and software development. *Appl. Mech. Rev.*, 47:s80–s84.
- 806 [53] Vreman, A. W. (2007). Turbulence characteristics of particle-laden pipe flow.
807 *Journal of Fluid Mechanics*, 584:235–279.
- 808 [54] Vreman, A. W. (2015). Turbulence attenuation in particle-laden flow in smooth
809 and rough channels. *Journal of Fluid Mechanics*, 773:103–136.
- 810 [55] Weller, H. (2002). Derivation, modelling and solution of the conditionally aver-
811 aged two-phase flow equations. *Tech.Rep.OpenCFD Ltd*.
- 812 [56] Weller, H. G., Tabor, G., Jasak, H., and Fureby, C. (1998). A tensorial ap-
813 proach to computational continuum mechanics using object-oriented techniques.
814 *Computers in Physics*, 12(6):620–631.
- 815 [57] Yamamoto, Y., Potthoff, M., Tanaka, T., Kajishima, T., and Tsuji, Y. (2001).
816 Large-eddy simulation of turbulent gas-particle flow in a vertical channel: effect
817 of considering inter-particle collisions. *Journal of Fluid Mechanics*, 442:303–334.
- 818 [58] Yu, K., Lau, K., and Chan, C. (2004). Numerical simulation of gas-particle flow
819 in a single-side backward-facing step flow. *Journal of Computational and Applied*
820 *Mathematics*, 163(1):319 – 331. Proceedings of the International Symposium on
821 Computational Mathematics and Applications.

- 822 [59] Zalesak, S. T. (1979). Fully multidimensional flux-corrected transport algo-
823 rithms for fluids. *Journal of Computational Physics*, 31(3):335–362.
- 824 [60] Zheng, Y., Wan, X., Qian, Z., Wei, F., and Jin, Y. (2001). Numerical simulation
825 of the gas-particle turbulent flow in riser reactor based on k- ϵ -kp- ϵ p- θ two-fluid
826 model. *Chemical Engineering Science*, 56(24):6813–6822.
- 827 [61] Zhou, X., Gao, J., Xu, C., and Lan, X. (2013). Effect of wall boundary condition
828 on CFD simulation of CFB risers. *Particuology*, 11(5):556 – 565.